INVESTIGATION OF THE SURFACE TOPOLOGY CHANGES ASSOCIATED WITH FATIGUE

BY

RANDALL KELTON

DISSERTATION

IN PARTIAL FULFILLMENT OF THE REQUIREMENTS

FOR THE DEGREE OF

DOCTOR OF PHILOSOPHY

THE UNIVERSITY OF TEXAS AT ARLINGTON

ARLINGTON TEXAS

May 2019

Dedication

This is dedicated to Maya, my wife and best friend. Thank you for always having more faith in the future version of me than I do.

Acknowledgements

First, I would like to thank my wife Maia Kelton. I would not have even dreamt of this without her support. I would also like to thank Dr. Efstathios I. Meletis, for giving me this opportunity in the first place. I would also like to thank Dr. Haiying Huang for being my most vocal critic, making me learn to question my preconceived notions. I would also like to thank Jalal Fathi and Kranthi Balusu for their guidance and support throughout the research work. I would like to acknowledge my group members for always being there when I need sound advice.

Abstract

INVESTIGATION OF THE SURFACE TOPOLOGY CHANGES ASSOCIATED WITH FATIGUE

Randall Kelton, PhD

The University of Texas at Arlington 2019

Supervising Professor: Efstathios I. Meletis

Metals have long been known to change their surface topology when subjected to a plastic strain. Given that a plastic zone exists at the tip of a propagating crack, it would seem natural to quantitatively study surface topology changes associated with nucleating and propagating fatigue cracks. So far the workers in this study have only found one measurement of the surface topology changes associated with a nucleating crack (1). The current research seeks to study and refine, a possible correlation between crack growth and surface topology changes, with the object to develop a damage index for fatigue cracking from surface topology measurement. The research uses a mechanical testing machine with an in-situ white light interferometer (WLI) which allows for high temporal resolution of surface roughness data. This research has demonstrated that certain aspects of crack propagation are associated with unique surface topology effects. It has also shown that WLI images can be used to develop a damage parameter which can predict the path of a propagating crack. Finally, using Electron Back-Scatter Diffraction (EBSD) techniques it has been shown that the damage parameter for propagating cracks is related to strain localization on the surface of a sample. For cracks initiating from a stress concentration the WLI methods developed in the current research have shown the ability to identify the location of a future crack even. This method has been shown

to work for initiation location even when no traditional strain localization features are present on the surface visible to the WLI, e.g. slip banding.

May 2019

Contents

List of Figures

List of Tables

Chapter 1 Project Motivation and Description

Recently many studies have been concerned with the surface roughness changes of both monotonically and cyclically strained samples. The studies concerned with qualitative analysis of topology related to fatigue cracks generally focus on the crack face surfaces. Virtually no research has been conducted on the changes in the surface of the material through which a crack is propagating. It has long been recognized that two plastic zones are developed around the tip of a fatigue crack, a monotonic and a cyclic plastic zone, as seen schematically in Figure 1-1 (2). Though this plastic strain has long been known to proceed the crack tip, little work has been done on the subject of surface topology changes associated with nucleating and advancing fatigue cracks.

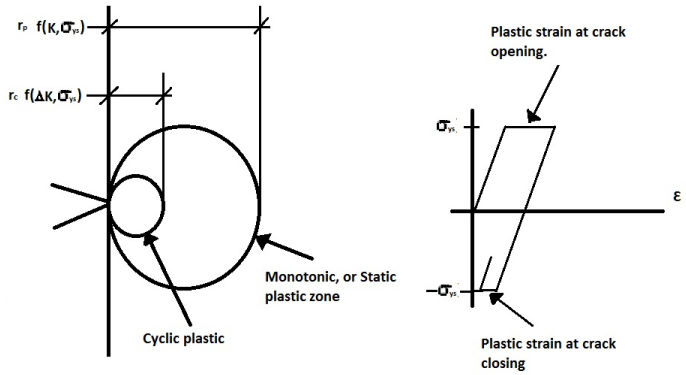

Figure 1-1 Schematic representation of static and cyclic plastic zones.

Specific features have been seen for both cyclic and monotonic strain. While these effects have been studied in literature (3) (4), work from the current study has shown monotonic plastic strain is dominated by grain level movements and more importantly for fatigue

cracking, cyclic plastic strain is dominated by changes within grains and triple points. For this

(1)

$$E = -E^{\sigma}_{app}(\sigma, m, L, N) - E_{hard}(\rho, L, N) + E^{dis}_{pile-up}(h, d, L, N) + \left(E^{dis}_{nuc} + E^{GB}_{ext}\right)(n, \Sigma, h, L, , L, N) + (E_{app} + E_{\gamma})(L, \gamma, N)$$

reason it seems natural to study the surface morphology changes of a sample associated with fatigue cracks.

In FCC material systems crack initiation and stage I growth have long been known to be closely associated with Persistent Slip Bands (PSB). In the last decade crack growth criteria based on the energy contained in PSB have been developed. These models suggest crack initiation, and by extension stage I growth, i.e. cracks passing grain boundaries, are a function of several quantities which cannot be measured. These factors include the Schmidt factor, along with size and grain boundary character of all neighboring grains. Currently, only the Schmidt factor and grain boundary character of surface grains is measurable via Electron Back-Scatter Diffraction (EBSD). For this reason these models have not performed well in determining crack initiation in practical materials. Also, the current research suggests the interaction of grains with neighbors is very important to crack initiation. While crack prediction models do not accurately predict specific conditions, they do predict the statistical spread seen in experimental data quite well. The model by Sanged et al (5) develops a relation for the energy contained in a PSB as a function of several parameters, most of which are functions of the geometry and orientation of the grain to be analyzed and its neighbors, as seen in equation 1. Each expression in equation 1 is expressed as a function of slip, thus the failure criterion is defined as $dE/dx = 0$ and $\frac{d^2E}{dX^2} > 0$. Figure 1-3 shows dE/dX plotted as a function of cycles

for two grain geometries. In this Figure, the blue line is associated dislocation multiplication, the red line is a function of the work done by extrusions penetrating the grain boundary and the black line is the total. It can clearly be seen that the energy from dislocation multiplication saturates, and soon after it is the energy of extrusions which drive dE/dX to the failure criterion. This is an important development because it implies a function of the failure criteria is directly measurable on the surface of cyclically fatigued grain in the form of extrusions.

Thus, the areas within the cyclic plastic zone most susceptible to fatigue cracking may have a measurable surface roughness index which could indicate the nature of the crack propagating within the part, and provide a useful damage index for predicting crack nucleation and stage I growth.

The following specific goals are intended to support the above hypothesis.

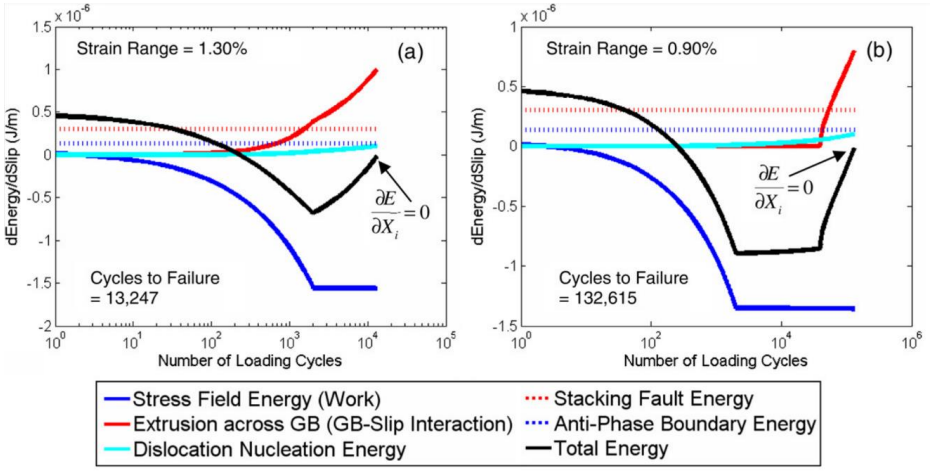

Figure 1-2 Contributions to total energy balance for two grain boundary configurations. Blue line related to energy from dislocation density, red line related to energy due to PSB extrusions into neighboring grains (5).

1. **Develop a white light interferometer (WLI) based damage index which can predict the propagation of a pinned crack tip and crack initiation location.** It will be shown

by work already completed that the total change in surface roughness around a pinned crack is monotonically increasing in an area local to the crack tip. This increase is shown to be more or less of the same magnitude for all pinned crack locations and not a strong function of the number of cycles, or stress intensity factor range, ΔK. Thus, the changes in surface roughness at a given crack pinning location is a function of local conditions. The number of cycles remaining for a crack to be pinned may be predicted from the amount of surface roughness changes compared to some threshold. For cracks initiating at a stress concentration the WLI damage index can accurately predict the crack initiation location even when no slip banding is seen on the surface.

2. **Develop a procedure to use surface roughness measurements to predict the path of a stage I propagating crack.** A local minimum in the surface topology changes was seen to precede the crack. This minimum was also observed to have the highest change in surface roughness indexes within the cyclic plastic zone. After growing the crack past a reference point, difference images were calculated from images taken while the crack was pinned several um before the reference point. With the future path of the crack known, arithmetic mean deviation, ΔSa and root mean squared deviation ΔSq were calculated for subsets close to and far from the future crack path. It was found that surface index values are highest along the future crack path and vanish away from the crack. This observation was used to create a procedure for calculating the future path of a propagating crack with good accuracy for up to 80 um.
3. **Validate via EBSD that the WLI damage index detects the area ahead of the crack tip with the highest cumulative strain.** It is hypothesized that the WLI damage index is

measuring surface roughness changes associated with the grains most favorably oriented for cyclic strain leading to stage I cracking along PSB. In order to verify the changes measured by the WLI are those areas with the highest strain, WLI images correlating surface roughness changes ahead of crack tip to EBSD images of the same were taken. EBSD Kernel techniques showed that while strain immediately adjacent to the crack was similar in propagating and pinned cracks, pinned cracks had a larger volume of highly strained material in the bulk leading to higher strain energy per unit length of crack at pinning locations.

Chapter 2 Literature Review

2.1 Background

Fatigue in structures has been studied now for over a century. In the late 1800's Wohler was the first to quantify fatigue through the creation of S-N curves. In 1910 Basquin (6) described these curves empirically. In the 1920s, ideas leading to the development of fracture mechanics emerged, starting with Griffith's theory and the burgeoning understanding of dislocation mechanics (7). The basic ideas of fracture mechanics were formalized in 1954 and widely accepted by the early 1960's after the Comet disaster. Despite this long pedigree of study fatigue still has a significant impact today. For instance still in the aircraft industry, fatigue in thermal barrier coatings leads directly to lower engine operating temperatures (8). Also, the need for tear straps and lap joint doublers significantly increase airframe weight (9).

Fracture mechanics was an important development for the study of crack growth. Soon after its formalization, crack growth rates were shown by Paris et al to be a function of ΔK, not simply stress (10; 11). Fracture mechanics now provided a parameter separating the threshold between the two common types of crack growth.

A plastic zone has long been known to be associated with the tip of the crack, and once again fracture mechanics provided a convenient tool evaluating the size of not only the

size of the monotonic (12), but also the cyclic plastic zones (13). These plastic zones are what may make characterization of a surface roughness damage parameter possible. What follows is a review of the topics important to the current research.

2.1.1 Fracture mechanics

Though as a discipline fracture mechanics is quite young, engineers have long been concerned with fracture. Leonardo Di Vinci was one of the first to demonstrate the size dependence of the fracture strength of steel bars (14). Despite Galileo's theoretical proof, a century later, that the strength of a beam should be proportional only to the cross section, the size effect remained an engineering concern for hundreds of years. Griffiths theory, was not only a step in explaining the size effect, it was one of the first steps toward the modern understanding of fracture mechanics. Ultimately advancements in continuum mechanics and dislocation dynamics lead to a canonical set of fracture mechanics tools (7).

By 1954 Irwin had formalized most of what is considered today to be fracture mechanics, focusing on three main tenants (7).

1. The leading edge of the crack tip
2. The energy for crack extension was taken from the elastic stress field
3. The plastic deformation near the crack tip that provides resistance to crack extension

In order to focus on the crack tip, stress and displacement fields needed to be developed around an advancing crack. In order to simplify the analysis three types of loading are generally considered and more complex configurations are super-positions of these three standards. Figure 2-1 is a schematic representation of the three standard crack tip loading modes I- Opening, II- Sliding and III- Tearing. In the current research the samples are designed to be loaded in mode I, so following development of fracture mechanics ideas will focus on mode I.

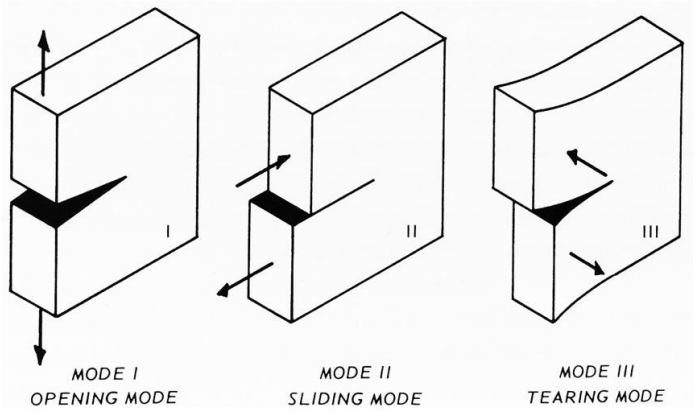

Figure 2-1 Three types of crack tip loading (http://thediagram.com/12_3/thethreemodes.html).

Irwin found the stress fields in the vicinity of a crack to be given by equation 2, with a coordinate system as seen in Figure 2-2.

These equations show the elastic stress at the crack tip, for a given type of loading, can be represented by a single parameter, K. Inspection of Equation 2 shows that stress intensity factor must be proportional to the square root of some characteristic

(2)

$$\begin{Bmatrix} \sigma_x \\ \sigma_y \\ \tau_{xy} \end{Bmatrix} = \frac{K_I}{\sqrt{2\pi r}} \cos\frac{\theta}{2} \begin{Bmatrix} 1 - \sin\frac{\theta}{2}\sin\frac{3\theta}{2} \\ 1 + \sin\frac{\theta}{2}\sin\frac{3\theta}{2} \\ \sin\frac{\theta}{2}\cos\frac{3\theta}{2} \end{Bmatrix}$$

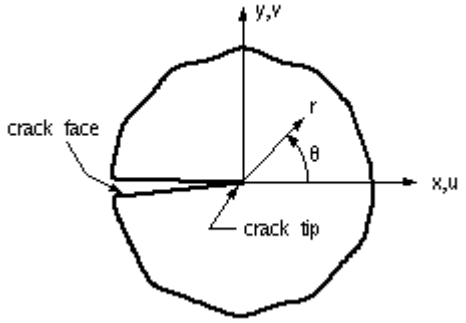

Figure 2-2. Mode I crack tip reference system.

length. Griffiths analysis of crack extension in glass tubes, demonstrated crack length as this characteristic value (12). Ultimately this leads to an expression for K which is directly proportional to the far field stress and the square root of the crack length. There will also be a factor which is proportional to the geometry of the sample, and possibly crack length as well. This leads to a relation seen in equation 3. In equation 3 a is the crack length, and f(g,a) is a function of geometry and sometimes crack length.

(3)

$$K = f(g,a)\sigma\sqrt{a}$$

There has been a tremendous amount of work on determining f(g,a) for various crack geometries and solutions which can be found in literature. For convenience, in the current study an ASTM center crack specimen was used so as to simplify the calculations of K and ΔK.

Two plastic zones have long been known to precede propagating fatigue cracks. First a monotonic plastic zone, where the material is tensely strained ahead of the crack tip. While there are several expressions for the size of the monotonic plastic zone, measurements made in the current research correlate best with the first approximation as presented by setting σ_y in equation 2 equal to the yield stress, $\theta = 0$ and simply solving for r (12) leading to equation 4.

(4)

$$r_y = \frac{1}{2\pi}\left(\frac{K}{\sigma_{ys}}\right)^2$$

Within the monotonic zone, and just adjacent to the tip of the crack is the cyclic plastic zone. Here, there is not just a tensile component to plastic strain, but also a compressive component. From measurements in the current study the size of the cyclic plastic zone was found to correspond well to the first approximation of the cyclic plastic zone as seen in equation 5 (13).

(5)

$$r_y^c = \frac{1}{2\pi}\left(\frac{\Delta K}{2\sigma_{ys}}\right)^2$$

Ultimately fracture mechanics allowed for a drastic simplification of study of fracture as will be seen in the next section.

2.1.2 Paris' Law and the da/dN curve

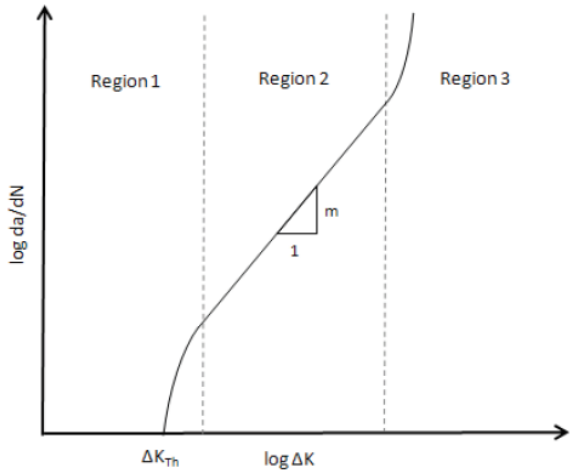

Figure 2-3. Schematic representation of da/dN curve.

Paris showed that crack growth rates are a function of ΔK. Figure 2-3 (15) is a schematic representation of da/dN plotted versus the $Log(\Delta K)$, and exhibits three regions. Region 1 is slow crack growth and is associated with stage I cracking as defined by Suresh (16), while region 2 is associated with stage II cracking. Finally region 3 is rapid unstable crack growth and rapid failure.

The boundary between regions 1 and 2 is known as ΔK_{th}, thus crack growth in region 1 is often referred to as sub threshold growth. This is a technically important region because, between nucleation and growth, up to 90% of part life can be spent here.

There is currently a tremendous amount of research concerning sub threshold growth; however, no simple relation such as Paris' law has been developed as it has for region 2. In region 2, Paris's law is valid and governs stable crack growth. Here the crack grows relatively quickly, but is more or less predictable due to Paris' law. Despite generations of research, the understanding of cracking in region 2 remains empirical. Many researchers have naturally used models based on dislocation and fracture mechanics to develop deterministic da/dN models based on bulk material properties (17). These deterministic models do lead to a power law dependence on ΔK^2, which agrees with dimensionless variables analysis showing that if Paris' law was based solely on bulk material properties, it should be proportional to ΔK^2 (18). Unfortunately, this relation could never be general enough to account for the variety of ΔK exponents seen in literature, thus it is likely crack growth is not simply governed by bulk properties. Region 3 is associated with rapid unstable crack growth and begins when ΔK rises close to the fracture toughness of the material. Thus, the boundary for region 3 is close to K_{Ic} of the material.

2.1.3 Monotonic plastic zone

The focus of the current research is on surface roughness changes of commercially pure Ni ahead of a fatigue crack. For this reason, the discussion of behavior will be focused on FCC crystal structures. As discussed in the section on fracture mechanics, a monotonic plastic zone precedes the crack tip as it grows; therefore, the crack is always growing through material which has been plastically deformed in tension. The classical representation of slip in single crystals is depicted as blocks of undeformed lattice sliding relative to one another (13), like a

deck of cards. This form of deformation has several important implications on the surface roughness changes relative to monotonically strained FCC poly-crystalline material.

First, slip escaping from the surface of a grain does so in the form of slip steps as seen in Figure 2-4 for monotonic loading. The shape and size of these slip steps has been seen to be a function not only of strain, but also on the orientation of the grain being observed (19). It has been observed in the current research that all grains within a monotonically strained sample do not contain slip steps, and even fewer grains are saturated over their entire surface. Thus, in monotonic loading, slip steps are not the main contributors to overall surface roughness changes.

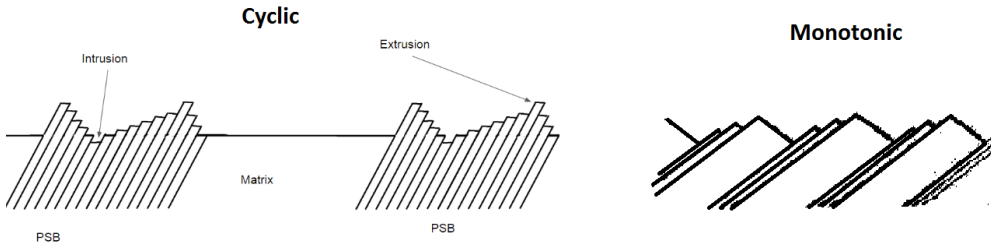

Figure 2-4 Schematic representation of Cyclic slip bands and Monotonic slip steps.

Strain hardening rates in single crystals are known to be orientation dependent (20). The current research has shown that different grains within the bulk do in fact accommodate differing amounts of strain in the tensile direction. This orientation anisotropy of strain and strain hardening rate (21) gives rise to long range stress concentrations, mainly at triple points and grain boundaries in poly crystal samples. It has been shown that grain boundaries and

triple points do in fact contribute the most to the overall surface changes in monotonically stressed samples (3).

2.1.4 Cyclic plastic zone

Within the monotonic plastic zone there are not only stress concentrations due to anisotropy of differently oriented grains, there is an isotropic stress concentration. The boundary of the monotonic plastic zone can be shown to be at or near the yield stress. In order to balance this stress concentration a residual compressive stress is developed at the root of the crack. This area of compression has a tendency to create an area of reverse flow even in tension-tension tests. The boundary of this reverse flow is the cyclic plastic zone and is the mechanism by which fatigue cracks grow (16). As seen before fracture mechanics offers a good estimation of the size of the cyclic plastic zone. And while the cyclic plastic zone is not circular as shown in Figure 1-1, experiment has shown that the transition from Paris region 1 to region 2 tends to happen when the cyclic plastic zone size is on the order of the grain size (13).

Within the cyclic plastic zone, crystal rotation no longer takes place thanks to dislocations being driven forward, and back, in the reverse direction. This leads to an eventual saturation of dislocation density (22) at a much higher density than that of monotonic samples (16), ultimately leading to a higher contribution from intrusion and extrusion to the measurable surface indexes. Also, due to the lack of crystal rotation and strain development in the tensile direction, local stress concentrations are not developed by cyclic strain, in fact cyclic strain has been seen to relieve local stress concentration created via monotonic loading (23). In the current research for moving cracks extrusions, where seen to be the major contributors to

surface roughness, increases. However, pinned cracks were seen to increase surface roughness at the triple point closest to the pinning location.

2.1.5 Stage I and II crack growth

Figure 2-5 is a schematic representation of stage I and stage II crack growth. Stage I growth is generally characterized with the zig-zag crack path seen when the plastic zone surrounding the crack tip is less than a few grain diameters. This type of growth is associated with single slip and, similar to PSB, the cracks tend to form along slip system planes (16).

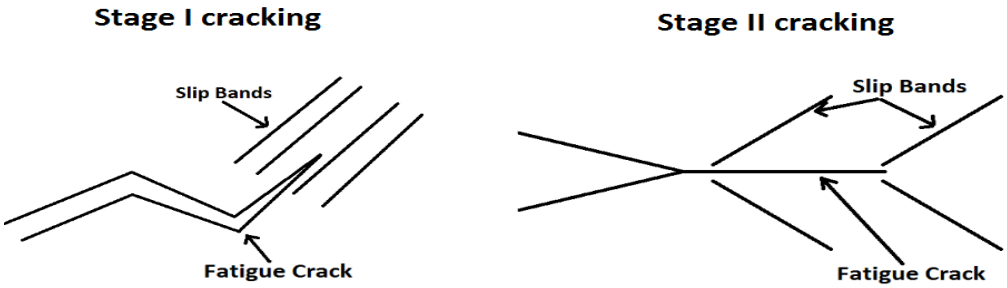

Figure 2-5 Schematic representation of stage I and II cracking.

Once the plastic zone grows large enough to encompass multiple grains, the crack enters stage II cracking. Here the crack is seen to grow perpendicular to the loading axis and slip can be seen on multiple slip bands (16). Several studies done with electron channeling contrast spectroscopy have shown that in stage II growth the tip of the crack is surrounded by cell structures (24; 25). Generally, dislocation structures start with the matrix material lacing cyclic deformations. Moving toward the crack tip from the monotonic zone, the first PSBs begin to form. From the edge of the PSB zone, wall spacing decreases, and dislocation density within the PSBs increases. Eventually, moving closer to the crack tip, PSBs transform to labyrinth

structure, as seen in Figure 2-6. Near the crack tip, labyrinth structures give way to cell structures and the crack progresses along cell boundaries, not microstructural features (24).

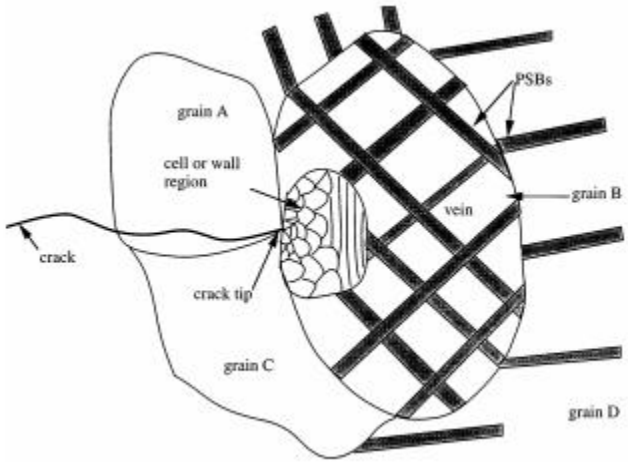

Figure 2-6 Schematic dislocation structures in front of the crack tips (25).

2.2 EBSD strain measurement

Dislocation structures in cyclically deformed samples have been shown to evolve as a function of the cyclic strain magnitude (26). While differences in orientation and neighboring grain interactions play a role in the dislocation structures initially formed, generally these structures progress toward cell type structures as plastic strain increases. This behavior has been reported in studies on the dislocation patterning preceding crack tips using the Electron Channeling Contrasts Imaging (ECCI) technique (24; 25; 27) as shown in Figure 2-6 ECCI has been shown to be able to directly image many types of lattice defects. For example, it has been shown, using ECCI that dislocation density is equivalent on both sides of a crack moving in a straight line, whereas in areas where cracks change direction the dislocation density differs on each side of the crack path (28). Dislocation structures have also been imaged using

ECCI. It has been shown that ECCI can image latter structures within PSBs similar to Transmission Electron Microscopy (TEM) though at a lower resolution (27). The changes in the dislocation patterning suggest cyclic strain is increasing toward the crack tip (29). As ΔK increases, the area of cells ahead of the crack tip grows larger. As stated before, it has been seen that locally, cracks seem to migrate along cell boundaries. This larger cell volume allows cracks to grow in the direction of the largest ΔK, rather than the highest Schmitt factor.

While the studies mentioned above used ECCI to study dislocation density structure around crack paths and tips, there are issues with using ECCI for the study of crack dislocation structures as the technique is sensitive to surface morphology. Any dislocation density observed with ECCI is only qualitative. Only dislocations at certain orientations provide sufficient contrast (28). ECCI is dependent on a two beam condition (30) thus; EBSD is often needed in order to orient each independently to maximize contrast for ECCI (31). Consequently, analysis of the interaction of cracks with multiple grains would be complicated with ECCI.

While EBSD may not have been yet used to directly image dislocation patterning, several EBSD methods have been shown to be related to strain. When strained, two types of measurable dislocations are created. Geometrically necessary dislocations (GND) which create a measurable axis rotation and statistically stored dislocation (SSD) which do not. Both types of dislocations have a similar effect on IQ, thus the use of Index Quality mapping can be used to qualitatively evaluate strain in poly-crystalline bulk (32). Kernel methods are directly related

to GND (33), and efforts to correlate EBSD kernel methods to dislocation patterning have shown some success (34) .

2.2.1 EBSD pattern analysis methods

While EBSD is often concerned with the analysis of indexed data, many possible damage indicators can be extracted from individual measured Kikuchi patterns. Attempts have been made to measure plastic and elastic strain by analyzing directly the information contained within the EBSD Kikuchi patterns. The sharpness of the lines in the patterns was an early focus of research to extract strain information. Early techniques consisted of simply comparing changes in line pair diffusivity by eye (35). These techniques were later refined using cross correlation and grey scale gradient across line pairs in images to directly measure strain from EBSD patterns (36; 37). Figure 2-8 shows the un-deformed and deformed EBSD diffraction patterns for a polycrystalline A316 stainless steel sample subjected to in-situ elastic tensile strain (38). As can be seen, the differences in image diffusivity across Kikuchi bands are quite small.

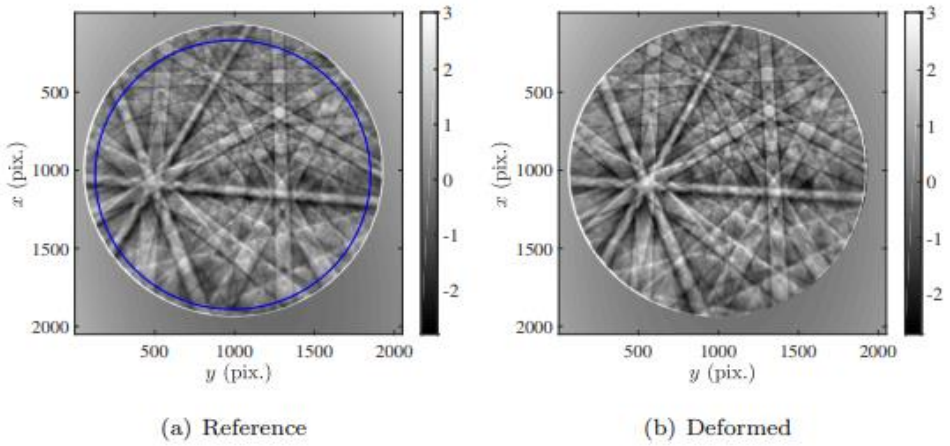

Figure 2-8 Image showing EBSD diffraction patterns for a) non- deformed and b) deformed A316 polycrystalline sample (38).

In order to overcome these small differences, techniques which essentially average these differences over several similarly oriented bands can be used (39). However, it is well known that the condition of the sample surface, independent of relevant experimental conditions, had similar yet much larger effects on the diffusivity of line pairs as stain (37; 32). Figure 2-9 shows the effects of surface preparation on Kikuchi line diffusion (32)

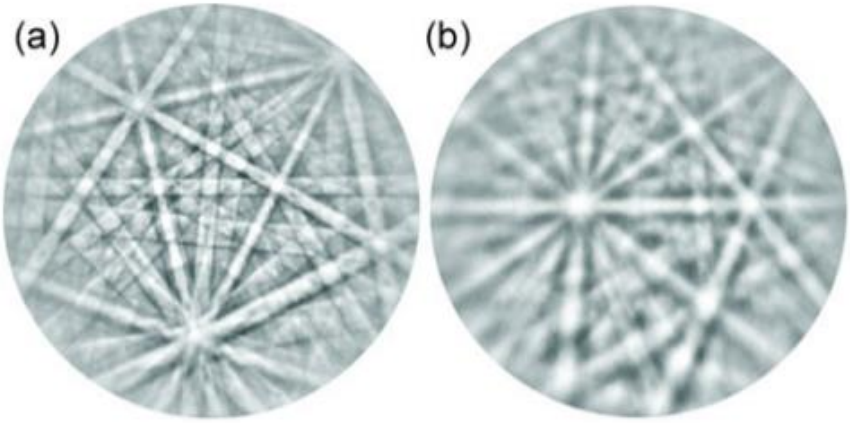

Figure 2-9 a) Well prepared surface b) Poorly prepared surface (32) .

The relative changes in diffusivity across Kikuchi patterns from strain and surface condition may be impossible to discern. More recent techniques add analysis of zone axis changes and potentially allow the direct measurement of the elastic strain tensor from analysis of the EBSD patterns (40; 41). However, these techniques rely heavily on the resolution of the CCD camera used to image patterns. In most commercial systems reasonable amounts of strain only create a difference of a pixel or two (32). It seems the lack of resolution of current EBSD systems has precluded automation of direct analysis of the EBSD patterns in current commercial EBSD systems (42).

2.2.2 Image quality methods

More commonly used measures generated from the EBSD Kikuchi patterns are the so called Image Quality (IQ) maps. IQ maps evaluate the entire EBSD pattern to return a given number representing the measured pattern for a given pixel location. The most ubiquitous of these is the parameter describing the average intensity of the peaks found in the transformation used to locate bands on the Kikuchi pattern. IQ_T is selected as to indicate the relative sharpness of each measured EBSD pattern (43). Mean Image quality IQ_m, standard deviation IQ_σ and entropy IQ_E were introduced in the early 2000s (44). The meanings of IQm and IQσ are straight forward; however, the meaning of the entropy, seen in Equation 6 (45) is related to the probability, P_i of each measured intensity value.

(6)

$$IQ_E = -\sum_{i=0}^{N-1} P_i - lnP_i$$

While it is obvious that IQ_E and IQ_σ are related, i.e. if the intensity of an image is Gaussian then the entropy will scale proportionally to the log of the variance. For this reason Tao and Eades

(44) suggested that $IQ_E \approx IQ_\sigma$; however, in the current research it has been seen that the histograms of EBSD patterns are often not normally distributed so that features may be visible in one map and not the other.

Previous work has shown that IQ_T can give a qualitative map of strain, and has high contrast with grain boundaries (46). IQ_M has been shown to be sensitive to phase and topography differences while IQ_E and IQ_σ contrast comes primarily through topography (42). Once again, as had been stated in literature and seen in the current research, these IQ parameters can be drastically affected by surface preparation, oxides, carbon deposition in the SEM, contamination… Thus these maps are qualitative at best, and may only suffice when no indexing is available.

2.2.3 Kernel methods

As stated before, when strained, two types of dislocations are created. Geometrically necessary dislocations GND create a measurable axis rotation, and statistically stored dislocations (SSD) do not. Both types of dislocations have a similar effect on IQ, and while it may be possible to use IQ for quantifying strain within a poly-crystal (32), recent studies suggest intra-granular resolution of IQ methods are not as effective as the kernel methods (34). Much like IQ methods, there are a plethora of kernel methods currently being applied, with an alphabet soup of acronyms (47), e.g. M_{ave}, MCD, GROD, KAM, GOS... Essentially, kernel methods quantify the differences in angle between indexed EBSD pixels within a given grain.

While there is a multitude of missorientation measures, two types seem to be most documented in literature relative to fatigue. These are Kernel Average Missorientation (KAM) and Grain Reference Orientation Deviation (GROD) (34; 48; 49; 50).

2.2.3.1 Kernel Average Missorientation

KAM is calculated by averaging the change in angle between a pixel and its n^{th} degree neighbors. Setting an angle threshold, e.g. 5°, (48) and excluding any neighboring grains above this threshold will ensure the high orientation across grain boundaries will not affect the calculations. Figure 2-10 shows a schematic representation of the calculation for KAM calculated for 1st degree neighbors. The black line indicates neighboring pixels with orientation deltas above the threshold. By finding pixels with missorientations above the threshold allows the KAM process to locate boundaries. Because KAM is calculated over a short range, its value is affected by the resolution of the EBSD measurement, thus for quantitative analysis all KAM calculations must be performed on Images taken at the same resolution.

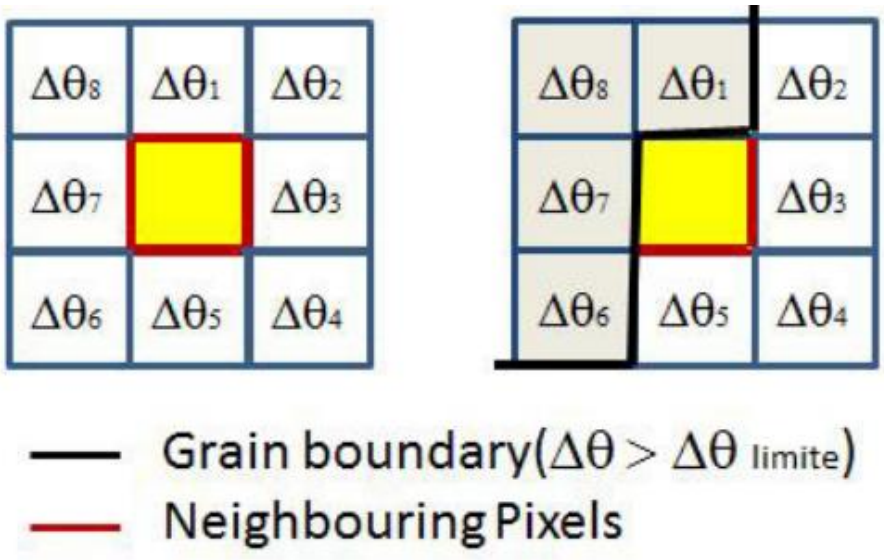

Figure 2-10. Schematic representation of KAM calculation. (48).

Because the contrast in KAM mapping arises from the missorientation of neighboring pixels due to lattice bending of strained grains within a poly crystal, it seems obvious that the larger the neighbor value, the higher the measured KAM value will be. However, it has also been shown that that the dependence of KAM values on the choice of n^{th} neighbors starts to diverge at around 3% true plastic strain (50), while the strain at the tip of a propagating crack stays below this level until very close to the crack (51). Therefore, 1^{st} neighbor KAM calculations are generally used in characterizing fatigue.

Finally, because KAM measures local crystal bending, it has been shown to be directly related to GND density per equation 7 (33). This allows for KAM to be a measurement of GND found at sites where strain localization occurs (52).

$$\rho_{GND} = \frac{2\theta}{ub} \tag{7}$$

Because KAM is insensitive SSD, areas of low strain have relatively low KAM values (53).

2.2.3.2 Grain Reference Orientation Deviation

GROD is another kernel orientation measure which has been used as a damage indicator for fatigue studies. It has also been shown to be a qualitative measure of dislocation density (54; 55; 32). For the GROD methods a reference orientation for each grain must be found. After finding a reference orientation, the angular difference between the reference and each pixel location is calculated. There are two main methods for finding the reference orientation. The method used by Kamaya finds the pixel within each grain with the lowest KAM, and uses that pixel orientation as the reference value termed Missorientation to a Common Direction (55). The more common method is to simply average the orientations of all the pixels within a grain, and use this as the reference orientation.

Chapter 3 Research Plan

3.1 Sample design and preparation

The current research investigations were done on the surface roughness evolution for both monotonic and fatigue samples. The following section describes the design and preparation of samples.

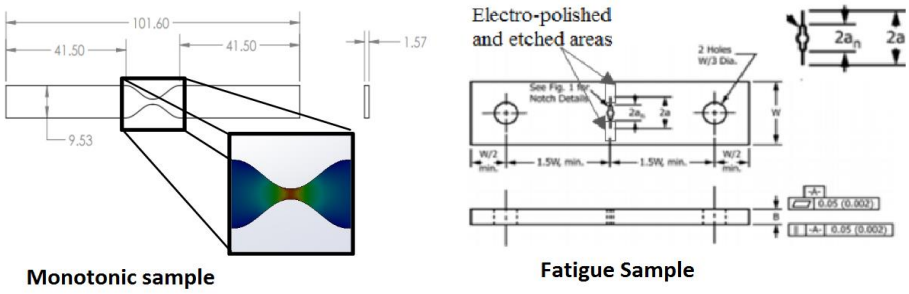

Figure 3-1. Monotonic and fatigue sample designs.

3.1.1 Sample design

For the monotonic experiment a sample was needed which would allow for the imaging of multiple grains at the same nominal stress state. Samples were machined starting with ASTM E8/E8M-13A sub size specimen dimensions as shown in Figure 3-1. In order to allow EBSD images and WLI tracking of all grains in the gauge area, the gauge area was reduced to 1.5X0.5 mm. Finite element analysis of the redesigned gauge area was performed to ensure a consistent stress state throughout the nominally designed gauge section. However, due to tolerances in machining, the actual sample measured a gauge width of 1.39 mm.

Fatigue samples were designed per the ASTM 647 center crack specimen requirements as shown in Figure 3-1. The center notches of the samples were machined with Electrical Discharge Machining (EDM) with a 0.254 mm (0.010”) wire per the ASTM 647 standard. For the initial fatigue experiments the dimensions as shown in Figure 3-1 are shown in table 1.

Table 1 Table of fatigue sample geometries.

	Length(mm)	W(mm)	2a(mm)	B(mm)	Grains size(um)
Initial Fatigue	98	17.77	4.8	1.52	89
EBSD/WLI	98	24.5	6.125	1.52	50

3.1.2 Sample preparation

Samples were machined from as-received commercially available pure Nickel sheet (Nickel 200, 99.52% pure, 1.575 mm thick). For initial experiments the grain size, measured per the ASTM E112-13 planometric procedure, was found to be 89 um. Samples were polished on both sides with conventional sand papers and alumina powders to achieve a mirror like finish. The gauge areas of the samples were then electro-polished in a standard Struers A2 solution at 24 V for 60 seconds. The electro-polished gauge areas were then etched in an ASTM E407 - 25 solution in order to reveal the grain structure. After electro-polishing and etching, the initial R_a before fatigue testing was approximately 120 nm for all samples.

For EBSD/WLI correlation experiments a new sheet of Nickel 200 was used with a measured grain size of 50 um.

3.2 Characterization

3.2.1 Electron BackScatter Diffraction

For over a century the fundamentals of diffraction as a characterization technique for crystalline materials have been known (56). By the late 1930s, the ideas originally developed for X-rays were successfully extended to electrons and the Transmission Electron Microscope (TEM) was commercialized by the early 1940 (57). Diffraction patterns have long been used in TEM to index crystals within samples; however, a more accurate technique is the use of Kikuchi patters.

X-ray diffraction and traditional TEM diffraction patterns rely on inelastic scattering. For electron microscopy these techniques image only electrons inelastically scattered at the exact Bragg conditions. However, as the sample becomes thicker, initially elastically scattered electrons have the opportunity for secondary elastic, higher order interactions. These elastically scattered electrons create a spectrum of electron energy, creating a range of Bragg conditions (58). This results in diffraction cones rather than points. While the majority of this elastic scattering happens in the forward direction, relative to the incident beam, there is some scattering in all directions (57; 59).

Electron backscatter diffraction is a technique which uses a scanning electron microscope's backscattered electrons to capture diffraction pattern information from a location of a sample. Samples are generally installed in the SEM at an angle to the main beam as seen in Figure 3-2.

A phosphor screen is used to collect the diffraction information. Because the backscattered electrons are coming from the surface of the sample the phosphor screen captures the backscattered Kikuchi pattern. A CCD camera behind the phosphor screen digitizes the pattern. The SEM beam is rastered over the sample surface to collect Kikuchi patterns at the desired resolution. Once a Kikuchi pattern is collected at each pixel location, the pattern is automatically indexed.

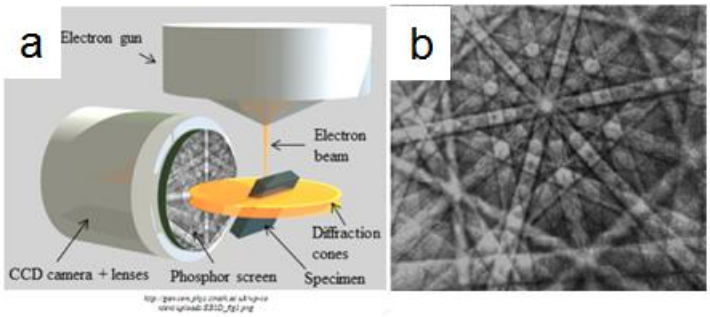

Figure 3-2. a) Schematic EBSD setup (58). b) Typical EBSD diffraction pattern (61).

3.2.2 Automated pattern indexing

The introduction in the late 1980s of automated Kikuchi pattern indexing helped the commercialization of EBSD (58). The general approach to automated indexing is to detect the major lines in an acquired pattern, and match those lines to theoretically generated patterns in a library (60). Often a process using a Hough transformation to identify lines in the original Kikuchi patterns is employed (61; 58; 60; 46); however, the NSS software used in the current research utilizes a general Radon transformation.

A Radon transformation maps an N, M image into x', θ space. The first step in this process, beginning at the center of the image, is to calculate a series of line integrals at different offsets from the center. The series of integrals is calculated at a specific angle to the horizontal as seen in Figure 3-3a (62). The calculation is then repeated over a range of angles. The dotted line in Figure 3-3a shows the direction along which the line integrals are computed. The intensity is then plotted for each angle, at each offset. Figure 3-3b shows two intense peaks at 90˚, at a plus and minus offset. The number of pixels in the Radon image gives the distance between these two lines, and the θ gives the lines slope relative to the horizontal. Figure 3-3c shows an actual EBSD pattern, with some corresponding Radon transform peaks indicated in Figure 3-3d.

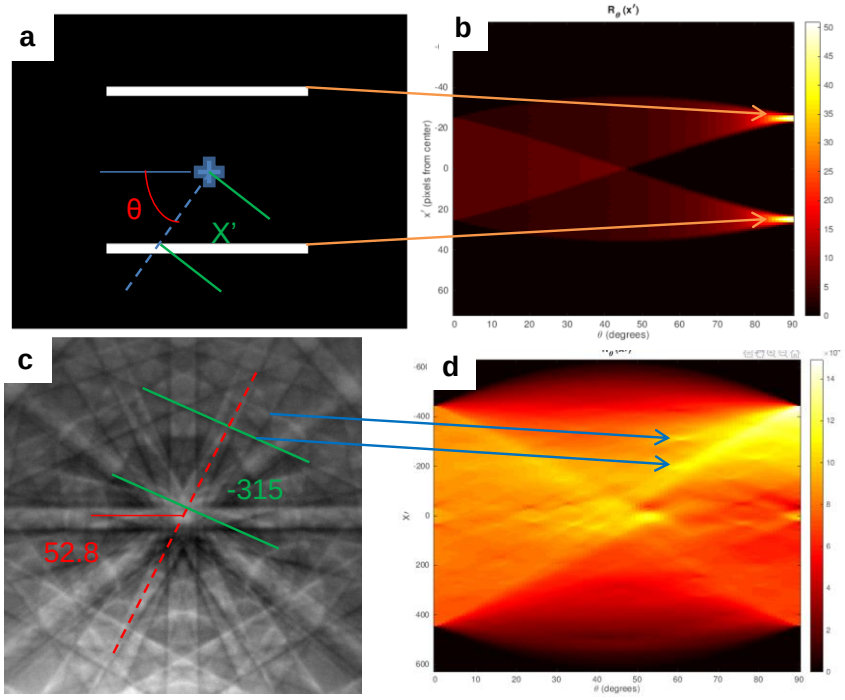

Figure 3-3. a) Stylized image with two lines. b) Radon transform of a. c) Actual EBSD pattern. d) Radon transform of c.

Once these peaks are found, the measured pattern can be matched with a pre-computed database for indexing (63).

3.2.3 EBSD system

The system used for the current research is a Thermo Scientific QuasOr EBSD installed on a Hitachi S-3000N SEM using Thermo scientific nss 3 software. EBSD mapping was conducted at 29 keV with a 70 degree sample tilt. For the sections of this study concerned with grain level orientation, a relatively low magnification of 230X allowed three images to cover the entire gauge area. Since electropolishing delivered a very high quality EBSD image, no "clean up" process was needed for analysis, and only the lowest level of clean up provided by the EBSD software was used for data presentation.

For the study of strain ahead of the crack, clean up could not be used due to the averaging techniques interference with strain measurements. Finally, for KAM and GROD analysis it has been shown that de-noising of EBSD data can significantly improve results obtained by EBSD mapping (64). De-noising as well as KAM and GROD calculations performed for this research used the MTEX toolbox available for MATLAB as described in (65).

3.2.4 White light interferometer

The ability of the WLI to measure abrupt changes in height on the order of the wavelength of visible light makes it valuable for a variety of research purposes, from simple measurements of step heights (66), to tracking the effect of production processes on the finished products (67). Interferometry using lasers has existed for quite a long time. However, when measuring features on the order of the wavelength of the light being used, ambiguities arise around

sharp changes in height. When multiple wavelengths of light are used this ambiguity can be greatly reduced (68). Figure 3-4 shows the interference pattern created by a white light interferometer as a sample point is transitioned through focus.

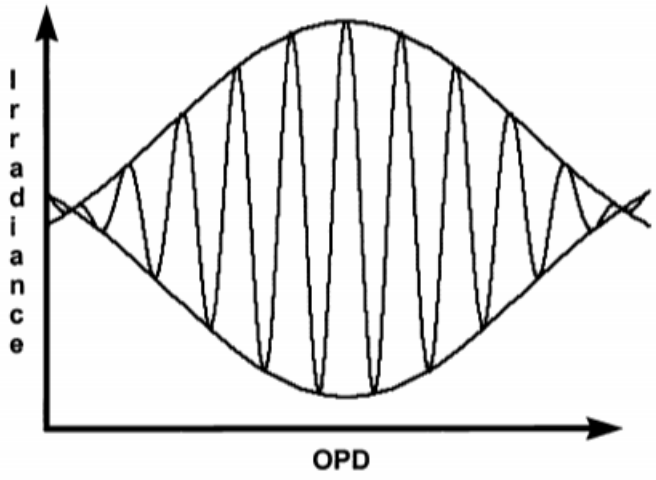

Figure 3-4 White light interferometry fringe intensity as a function of focus (68).

For a monochromatic interferometer, each peak would be at the same height. The benefit of WLI is that there is only one first order peak. This allows the measurement of fields of view with step heights large relative to any one wavelength of light. Figure 3-5 a WLI interference pattern measured on a mems device (69). Steps in the device can clearly be seen by discontinuities in the fringe pattern and the appearance of only one first order fringe makes the measurements of the steps unambiguous.

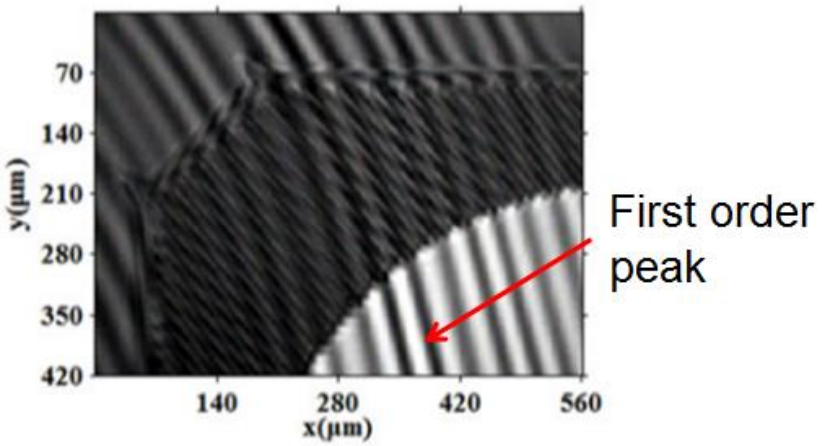

Figure 3-5 WLI fringes on MEMS device (69).

White light interferometry had already been shown to be useful in the study of fatigue induced surface changes (4). Together with the ability to stitch images over a relatively large area made the WLI ideal for the surface characterization of the present study.

For tensile samples, WLI images were taken with a Brunker NPFLEX at 20X magnification. In order to cover the gauge area, 12 images were taken and automatically stitched together by the Brunker Vision64 software with a 20% overlap. For fatigue samples, an area 3 mm X 1 mm around the crack tip (1 mm behind the crack to 2 mm ahead of the crack tip) was imaged at 10X magnification in order to measure the surface profile of the entire plastic zone. These WLI images were taken approximately every 5000 cycles while pre-cracking at a linearly rising ΔK. Upon reaching the surface viewing zone, an area 0.6 mm X 0.6 mm around the crack tip (0.1 mm behind the crack to 0.5 mm ahead of the crack tip) was imaged at 50X. These images contained 1640 X 1640 pixels leading to an x-y resolution of 0.366 um and a z resolution of 1 nm.

Chapter 4 Results and discussion

4.1 Tensile testing

In order to develop an understanding of the monotonic plastic zone preceding fatigue cracks, initial experiments for the current research were done on a sample which was monotonically plastically strained in tension. Samples were installed in a Bose LM2 Test Bench mechanical testing machine equipped with an in situ WLI. Initially, tensile tests were conducted on standard dog bone samples in order to determine the 0.2% yield and ultimate stress of the as received material. Figure 3 shows the measured stress strain curve. The yield and ultimate strengths were measured to be 211 MPa and 494 MPa respectively, which agreed well with those quoted in ASTM B162.9954.

The sample was subjected to stresses, increased by approximately 15% of nominal yield stress for each loading cycle. Between each loading cycle, a WLI image was taken. Though WLI images were taken at every 15%, no discernible changes in the sample were detected until 102% of the calculated yield strength. Beyond 131% of the yield strength, the WLI images started deteriorating quite rapidly leading to only four significant loading levels initial, 102%, 117% and 131% plotted in Figure 4-1.

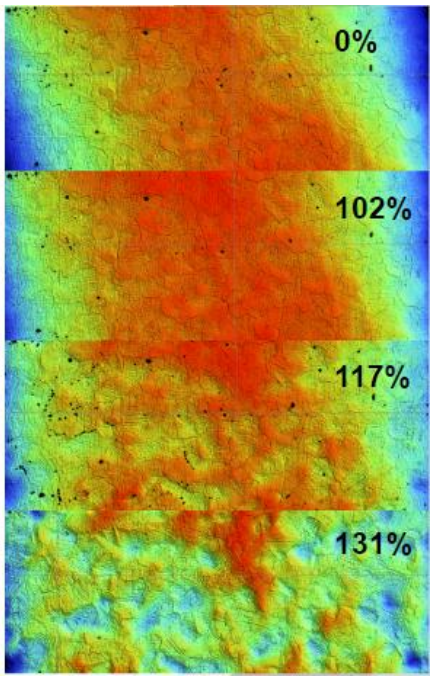

Figure 4-1. WLI images of tensile sample at 4 different stress levels. Percentages are percent of yield stress.

4.1.1 Grain level displacement.

The initial analysis was to determine the how orientation to the tensile axis effects a grain's contribution to surface roughness changes. In order to determine the areas of the gauge length which were rising or falling the most, a histogram for the pixel height of the WLI images was taken at each stress level. The histograms were used to calculate ± 2 sigma values of pixel height for each image. These values were used as threshold to create images showing only the areas of the sample which rose and fell the most at each stress level as seen in Figure 4-2 B. Once the images with rising and falling areas are calculated, the WLI and EBSD images can be indexed and the hkl indices of the loading direction for each grain can be found as seen in Figure 4-2.

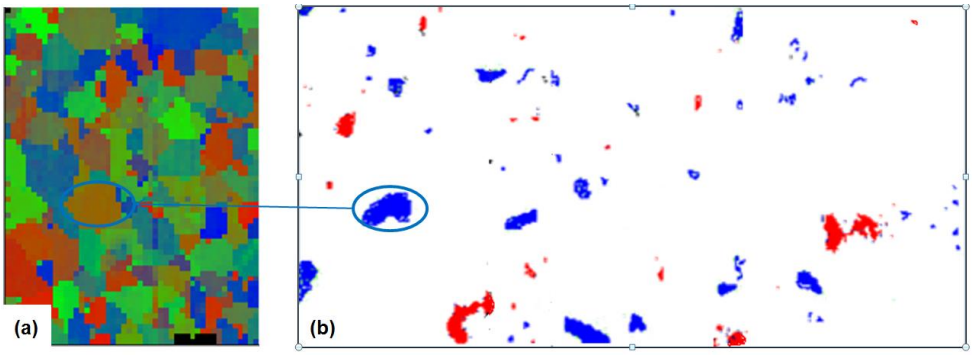

Figure 4-2. Indexing of WLI rising and falling data with EBSD data. a) EBSD data for base 1, and b) WLI rising and falling data.

Once the rising and falling grains were found, the hkl indices for their loading direction were calculated and plotted on the standard stereographic triangle. Figure 4-3 shows rising and falling grain locations in the stereographic triangle. The results show that the majority of the falling grains lie along the edges of the triangle, i.e. multi slip, while the rising grains congregate in the center, which is the single slip portion of the triangle. These areas roughly correspond to regions of the stereographic triangle found by Unger et al (21) for differentiation in grain level hardening vs. dislocation density in polycrystalline Ni.

In the current study, we define the single slip area of the stereographic triangle to be those tensile axis orientations which are closer to the [124] direction than to the [-100] or [0-11] planes. Grains closer to the [-100] or [0-11] planes are defined to be in the multi slip area of the triangle. Figure 4-3 shows this area roughly outlined in red.

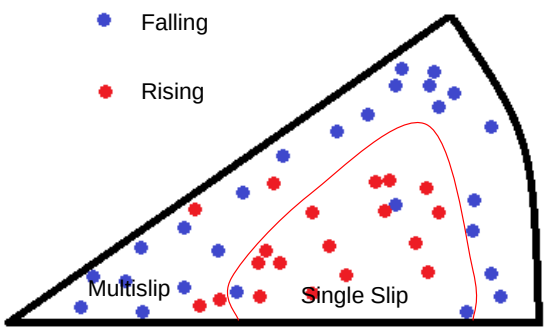

Figure 4-3. Inverse stereographic triangle showing typical rising and falling grain locations, and dislocation patterning sections of the stereographic triangle. There are a total of 24 falling and 18 rising grains.

4.1.2 Slip step development

Though some slip bands did develop early at 102% of yield strength, at 144% of the yield strength only 16 of the approximately 240 grains showed slip bands. Grains which did develop slip bands were not necessarily those which rose and fell most substantially. While some grains which did rise and fall large amounts showed slip banding, the contribution to surface roughness from slip bands was small relative to changes in overall grain geometry. Figure 4-4 shows the grain containing the largest slip band in the gauge area, which created a surface high change of only 0.25 um, while the height distribution for the area changed from 0.3 um to more than 1 um. This shows that in tension, even where slip bands appear, their contribution to overall surface roughness is not as high as that of grain level movement

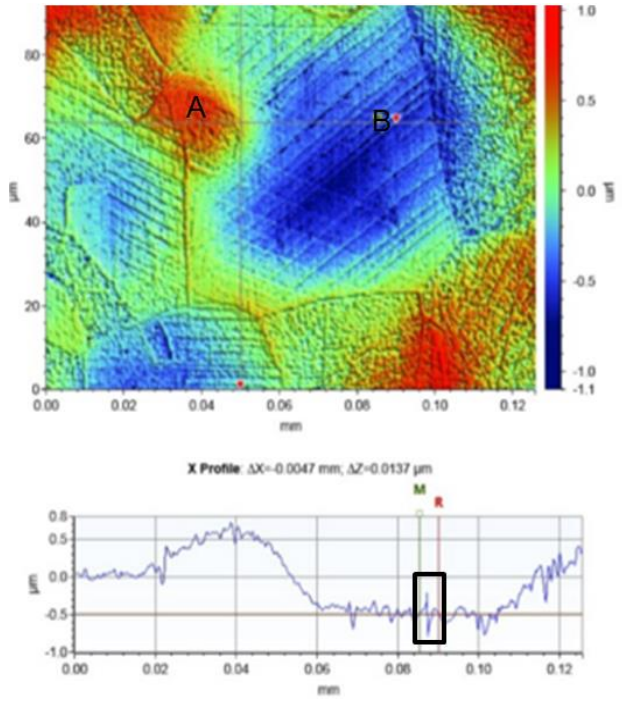

Figure 4-4. Images and line profiles of grain with highest slip band saturation after application of 24% strain.

4.1.3 Grain level residual strain

In order to measure the residual strain in grains after loading, the WLI software was utilized to measure the length of grains in the tensile direction initially and after each stress increment. As stress was increased, it became impossible to make accurate measurements for all grains so that each area was measured at least twice, and only grains with precise measurements were used. For this reason, only 13 grains could be utilized for strain measurements (seven falling and six rising) out of the original 49 identified rising and falling grains.

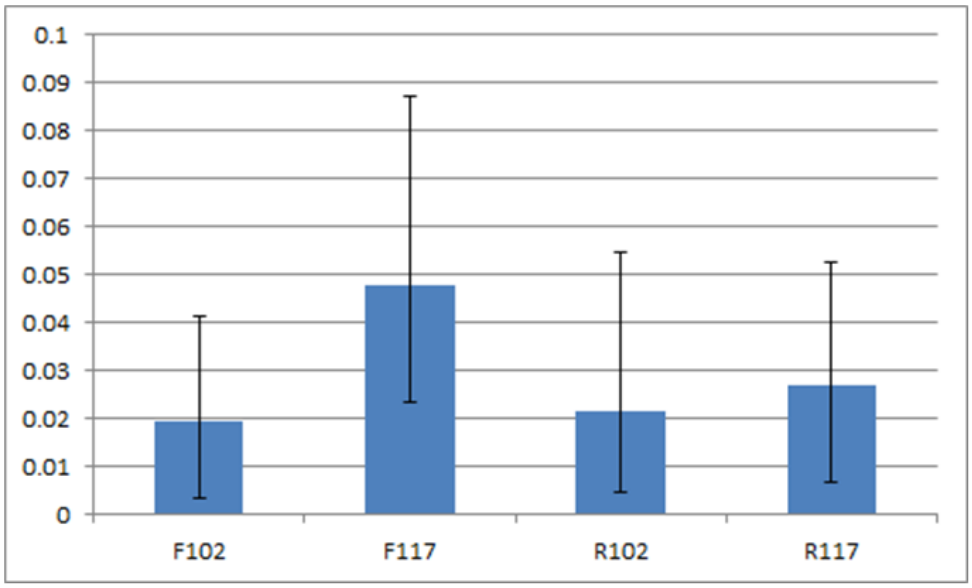

Figure 4-5. Residual strain after loading for falling and rising grains. Data are based on 7 falling and 5 rising grains.

Figure 4-5 shows the applied stress vs. residual strain after unloading, for rising and falling grains. It can be seen how the residual strain between the initial 102% yield and the 117% yield for falling grains is much higher than for rising grains. Because falling grains are primarily in the single slip zone of the stereographic triangle this strain is contrary to what would be expected in single crystals (70; 71). Grains accommodating differing strains have been reported in literature (4), as has tensile hkl dependent strain hardening. Ungar et al (21) reported a higher dislocation density hardening rate in single slip orientations within polycrystals as opposed to multi slip orientations. While dislocation density could not be calculated in the current study, a direct relationship between dislocation density and strain has long been recognized, suggesting a higher strain hardening rate for single slip tensile hkl in polycrystals.

4.2 Fatigue experiments

The current research employed a custom experimental apparatus which employed a Bose Test bench mechanical testing machine, with an in-situ Brunker NPFlex WLI as seen in Figure 4-6. This set up allowed for relatively rapid acquisition of WLI images without removing the sample from the testing machine. This allowed for not only high spatial resolution, but more importantly, high temporal resolution in WLI images ahead of fatigue cracks.

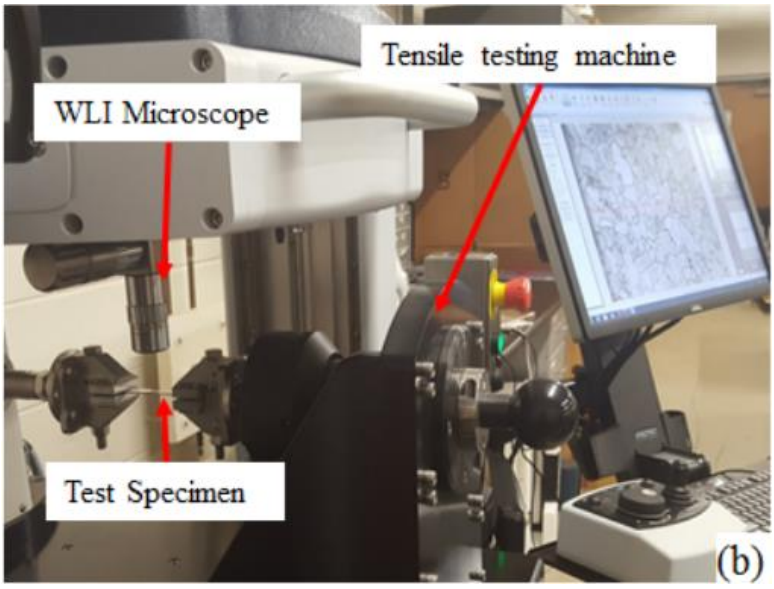

Figure 4-6. Bose Test Bench testing machine with in-situ NPFlex WLI.

Several reasons made the ASTM 647 center crack specimen ideal for this experiment. First, the relatively small size accommodated the maximum load of the Bose test bench, which can only apply ± 3000 N. Second, because this sample has two notches, compared to one for most other standard fatigue samples, it would allow for doubling the amount of data collected for

each experiment. Finally, the geometry parameter is well known, making calculation of the of the stress intensity factor simple compared to a custom designed sample.

the initial crack propagation experiment was designed to observe a fatigue crack interacting with several grains at a similar ΔK. The crack was grown in three stages, pre-cracking, crack growth before the surface viewing zone, and crack growth within the surface viewing zone, as shown in Figure 4-7. A minimum pre-crack length, Δa = 1 mm, was grown from the notch as per ASTM 647. The initial crack was nucleated by cycling at 10 Hz for 120,000 cycles. The crack was nucleated with a maximum stress intensity factor (SIF) and SIF amplitude of $K_{max} = \Delta K =$ 11.2 MPa$\sqrt{m}$. These values were allowed to rise linearly to $K_{max} = \Delta K$ = 13.1 MPa$\sqrt{m}$ at the desired pre-crack length.

Based on surface profile measurements on previous samples of the same geometry and loading schedules, the estimated crack-tip plastic zone had a size of 0.5 mm at K_{max} = 13.1 MPa$\sqrt{m}$. In order to ensure no plastic deformation effects from stage one pre-cracking affected measurements, a second controlled 0.5 mm pre-cracking stage followed. The later stage pre-crack was grown at a nominally constant $K_{max} = \Delta K$ = 13.1 MPa$\sqrt{m}$ at 10 Hz. The SIF was maintained by measuring the crack length and adjusting the load every at most 1000 cycles.

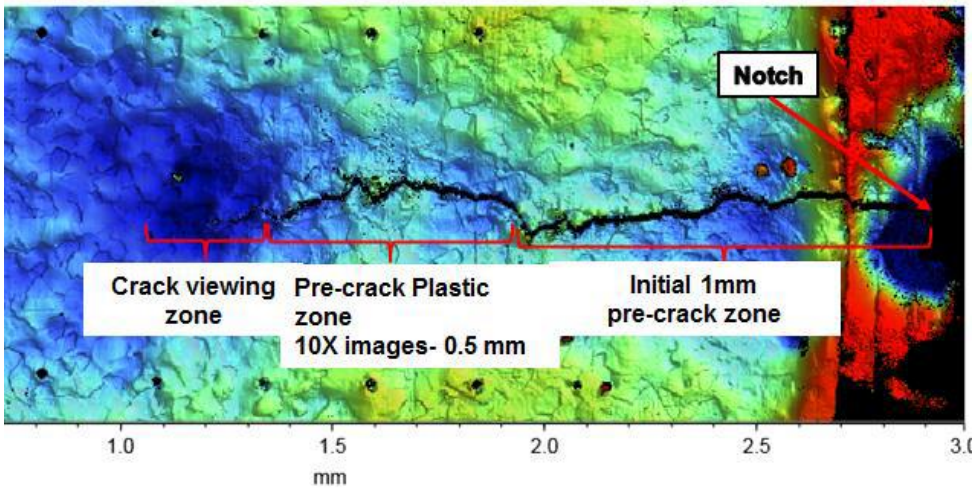

Figure 4-7. Plan view of the sample showing different crack growth zones.

Crack initiation and EBSD experiments were also conducted on center crack samples prepared similarly to the crack propagation samples above, only with a slightly different geometry as described and grain size as described in table 1.

4.2.1 Measurement of monotonic and cyclic plastic zones

Before beginning the high resolution imaging, the extent of the monotonic and cyclic plastic zones observable by the WLI was measured. This measurement was performed on a previous sample with exactly the same geometry and loading schedule. Once the crack reached the minimum crack length as per ASTM 647, the Ra and Rq, (root mean square roughness), values were calculated for an area 0.1 mm x 0.8 mm located 1.4 mm ahead of the crack tip as shown in Figure 4-8. The Ra and Rq values were calculated for this same area every 1000 cycles as the crack tip advanced at a constant nominal SIF amplitude of $\Delta K = 13.1$ MPa$\sqrt{m}$. Figure 4-8b shows the Ra and Rq value versus dx from the crack tip. Two distinct zones can be observed. First, a small rise in Ra can be seen approximately 0.5 mm in front of the crack tip, which is

considered to be the outer edge of the monotonic plastic zone. This equates well with the first approximation of monotonic plastic zone size, which was calculated to be 0.6 mm according to equation 4. Inside the monotonic plastic zone, there is a plateau where ΔRa changes very little. Within approximately 0.2 mm from the crack tip another rise in surface roughness was measured and assumed to be the cyclic plastic zone. Again, this agreed well with the theoretical size of the cyclic plastic zone, which was calculated to be 0.3 mm via equation 5.

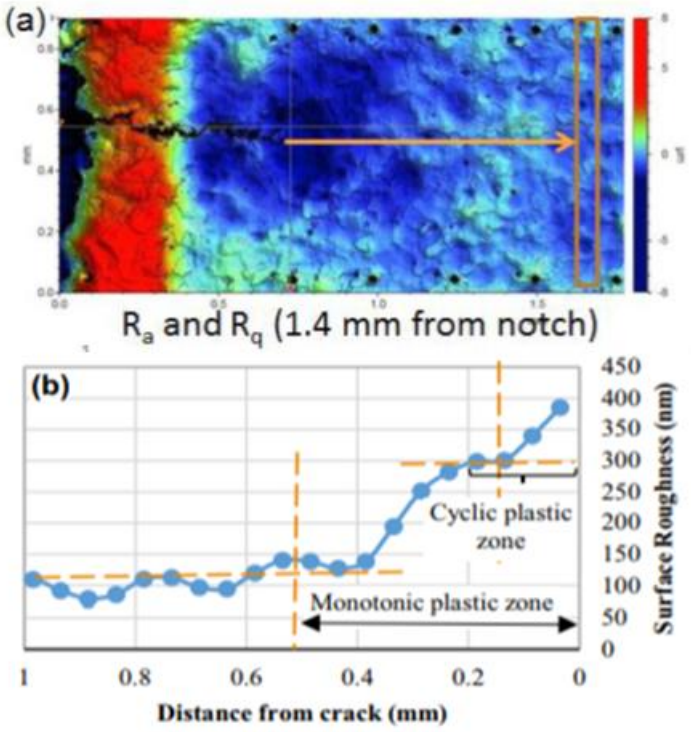

Figure 4-8 a) Area where S_a was calculated as the crack tip moved. b) S_a plotted as a function of distance from the crack tip.

4.2.2 Surface topology change, pinned and propagating cracks

In order to evaluate the surface morphology change as a function of fatigue cycles for both the moving and pinned cracks, a process that could quantify the difference in the topologies

captured by WLI at different fatigue cycles was developed. This process was then applied to study the surface morphology changes associate with crack. As will be seen, unique changes relative to both moving and pinned cracks were able to be characterized. It was theorized that the changes measurable by the WLI were ultimately consequences of strain localization relative to the crack tip. To correlate strain localization at crack tips with changes in surface roughness EBSD was used to investigate the crack wake containing propagating and pinned cracks.

4.2.2.1 Pinned and propagating crack surface morphologies

To calculate a difference image, WLI images must be registered so that the image pixel locations are aligned spatially. This required registration of WLI images to a common "world" coordinate system with a high degree of accuracy. The first step in image registration is to correctly account for tilting of the measured samples.

When measuring surface features with the WLI, the sample is not always placed in exactly the same position relative to the objective lens. These small variations in measurement conditions can create issues while trying to create difference images. Figure 4-9a shows a schematic of the types of experimental conditions between measurements which can cause issues when calculating difference images. First, the absolute z value will not be exactly the same from measurement to measurement. Second, slight differences in the imaging tilt can cause large difference image errors. Figures 4-9b and 4-9c show images of a 3D Gaussian bump. Figure 4-9b is the ideal bump with no tilt, while Figure 4-17c shows a slightly deformed bump, with

added tilt and a z offset. Figure 4-9d shows the difference image of b and c, without correcting for tilt and offset.

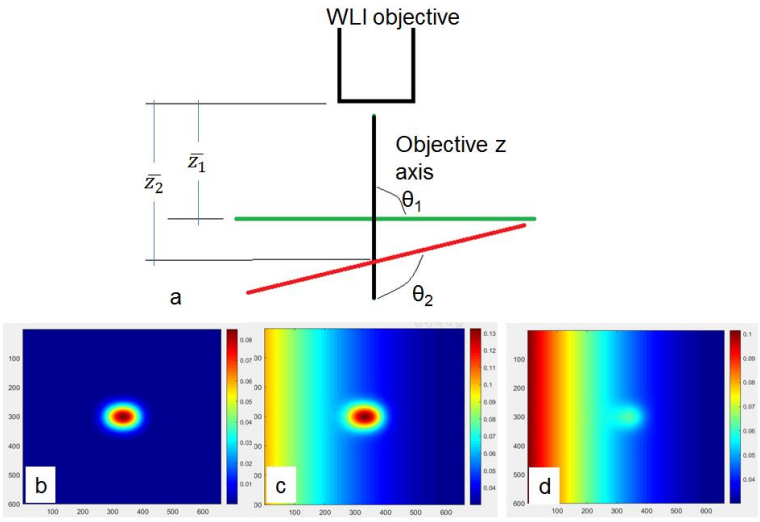

Figure 4-9 a) schematic of the possible WLI positioning differences which can cause issues in image registration. b) Gaussian bump. c) Deformed Gaussian bump. d) Difference image without tilt correction.

The largest differences visible in Figure 4-9d come not from the differences inherent to the feature of interest, but due to tilt and offset. Therefore before registration each image must be processed to remove tilt, and set a global height level. In order to accomplish this, an area of the sample which should be most stable, e.g. the elastic zone far from the notch is used as a mask, and tilt is corrected only using that area.

Figure 4-10 shows an area just ahead of the notch which was processed for the EBSD correlation studies described later. By default in the WLI software, images are tilt corrected using the entire image, and there is no adjustment of z offset.

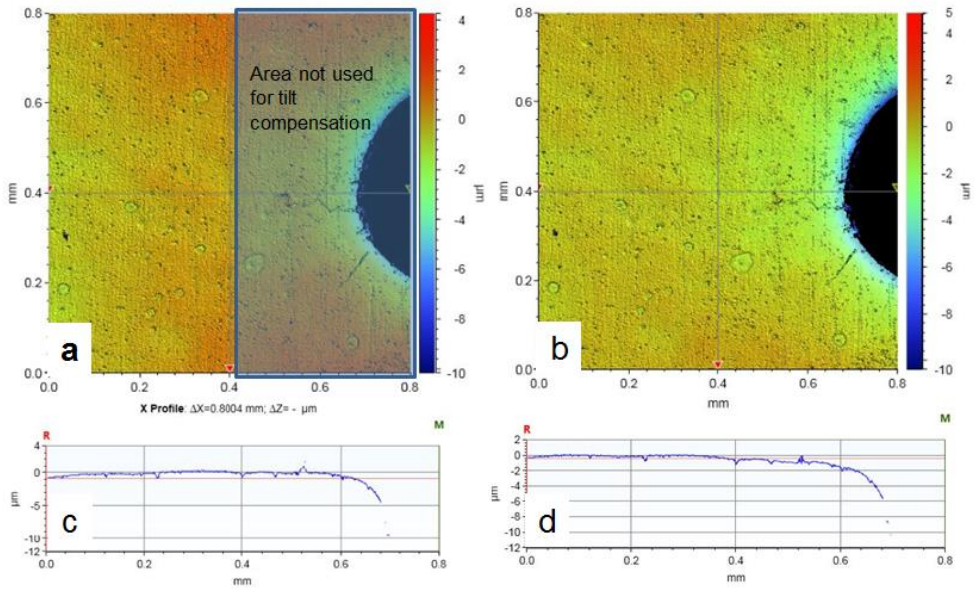

Figure 4-10 a) WLI image with default tilt correction showing the area masked for tilt compensation. b) WLI telt compensated to elastic area with corrected z offset. c) Cross section of image a. d) Cross section of image b.

Figure 4-10a is the image with default model tilt removed. The area containing the notch is then masked and tilt is recalculated. Once a new tilt is calculated the average height of the unmasked area is set to zero, as seen in Figure 4-10b. Figures 4-10c and d show the horizontal cross section on the line running through each respective image at 4 mm. While the absolute adjustment to the average height of the images appears small, this offset is large compared to the changes we wish to analyze in the difference images. Once tilt and height are normalized a method to register the images can be used.

This was achieved using the MATLAB computer vision toolbox, as well as a process involving Binary Robust Invariant Scalable Key points (BRISK) (72) and Speed (73). Once the images are registered, a simple difference image can be calculated as seen in Figure 4-11.

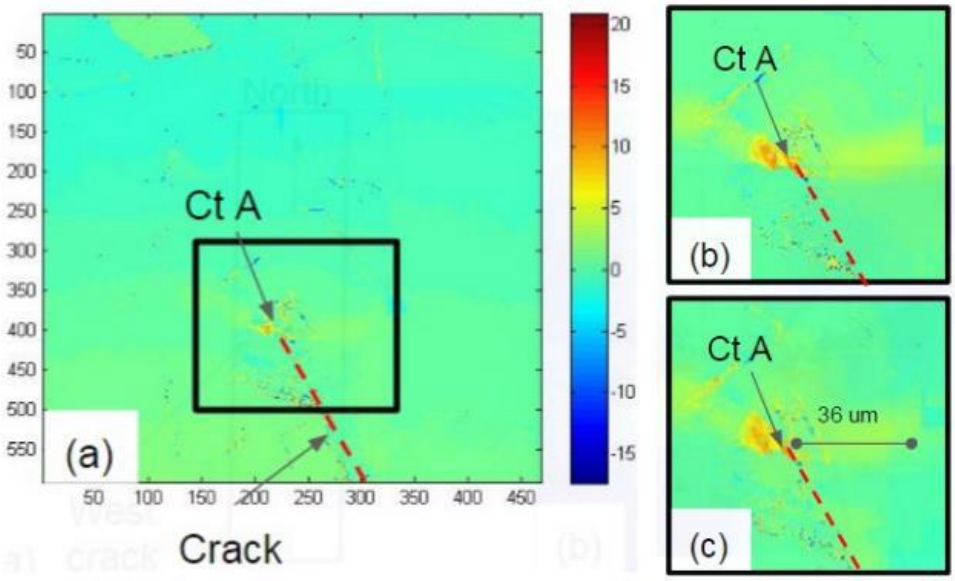

Figure 4-11. Difference images for crack tip location A a) 600 cycle, b) 1200 cycle and c) 1600 cycle image.

Fig. 4-12 shows a WLI image of the crack viewing zone for the “west” crack of the sample. In this image, the crack was pinned at points A, C, D, E and F for a considerable number of cycles. Each of the pinning locations was seen to be associated with large change in surface topology. The majority of surface roughness increase was coincident to the triple point closest to the pinning location.

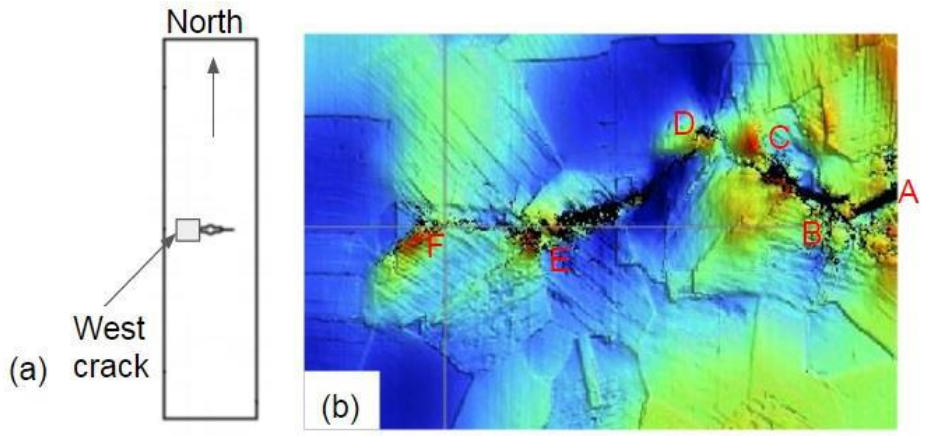

Figure 4-12. Location of the "west" crack a) Area of crack b) WLI of the crack viewing zone.

For pinned cracks distinct surface topology changes were seen. First, during the time the crack was pinned, significant surface roughness changes were localized within the cyclic plastic zone. Figure 4-11 shows three images for different numbers of cycles while the crack was pinned at point A. While surface changes can be seen around the monotonic zone, the highest changes are adjacent to the crack tip. Figure 4-11(c) shows that even after 1600 cycles, surface changes accumulated, but the pattern remained the same and the majority of changes were contained within approximately 40 um of the crack tip while the theoretical size of the cyclic plastic zone is on the order of 300 um. This suggests the surface roughness changes are restrained well within the cyclic plastic zone when the crack is pinned.

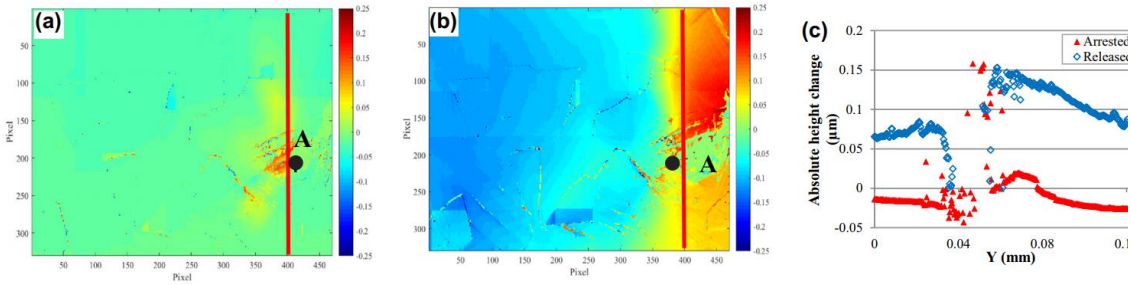

Figure 4-13 a) The 2000 cycle Difference image for the crack pinned at point A before being released. b) The 200 cycle difference image after being released from point A. c) The 2-D profile of difference images along the same cross section at the original point A for the arrested i.e. 2000 cycle image, and the released i.e., 200 cycle image (80).

When the crack was finally released from the pinning location, large changes in the surface topology can be seen throughout the monotonic plastic zone. Figure 4-13a shows the 2000 cycle difference image for the crack pinned at point A. Here as before relatively small surface roughness changes can be seen common to the cyclic zone of the pinned crack. Figure 4-13b shows the 200 cycle difference image once the crack was released from point A, after being pinned for 4000 cycles. Figure 4-13c shows the profile along the cross section common to point A for both the arrested and released crack tip. In this image, large differences extending over the entire registered image area can be seen as opposed to the local changes seen when the crack was pinned. In contrast, very little surface topology changes could be seen when cracks were propagating.

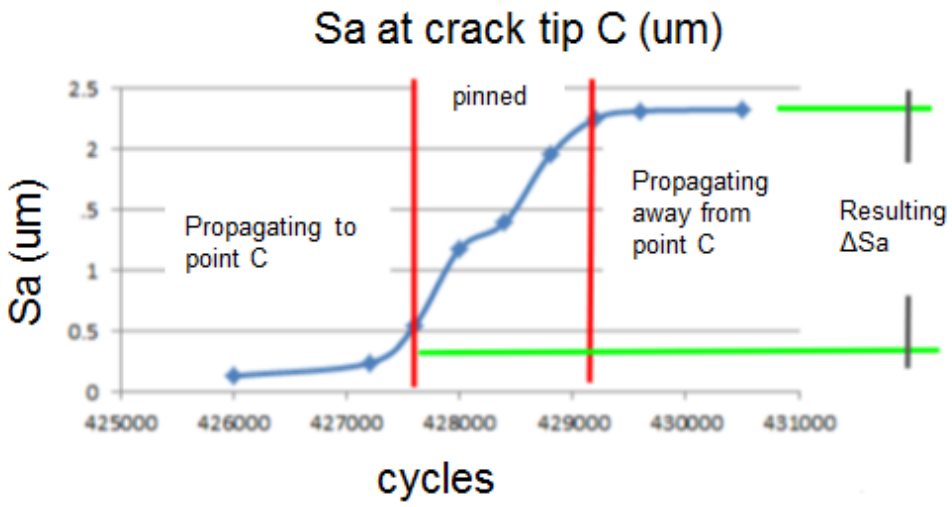

Figure 4-14. Ra vs cycles for crack pinning location C.

As was mentioned earlier, when the crack was pinned for any number of cycles, a small mound was created, either at the crack tip, or a nearby area. In order to compare the topology evolution at each location, the total change in R_a was calculated for the areas containing the mounds at each pinning location. The R_a of the mound when the crack was pinned at point C is plotted versus the fatigue cycle in Figure 4-14. The results show that when the crack is pinned at point C, the surface roughness continuously increases until the crack is released. It is interesting to note that no roughness increases are seen prior to or after the pinning process. We found this behavior to be typical for other crack arrest sites. This behavior is typical of all mounds built during crack pinning.

Table 2 also contains the propagation rate upon leaving each pinning location the and corresponding ΔK. It is interesting to note that though the number of cycles during which the crack was pinned at each location varies greatly, the absolute S_a change is similar for a given

ΔK. This similarity in ΔS_a may suggest a correlation between a surface roughness threshold for pinned cracks and ΔK.

Table 2. Data relative to each crack pinning location.

	Pinned Cycles	Resultant ΔS_a um	Velocity um/cy	ΔK $MPa\sqrt{m}$
A	4000	1.54	0.04	13.1
B	1600	1.7	0.012	13.1
C	500	1.96	0.04	13.1
D	800	2.61	0.069	13.4
E	1000	2.62	na	13.6

However, more investigation is needed to determine if these differences in ΔSa are correlated to ΔK or affected by conditions local to the crack tip (e.g., intergranular vs grain boundary effects, grain orientation, local K due to crack geometry, etc.). It should be noted that because the exact number of cycles at each pinning location is not known due to measurements being taken only every 200 cycles, the threshold from data in Table 2 is an average value.

The initiation of crack pinning could be determined from a sharp increase in S_a. The slope of the S_a versus cycles could then be combined with a threshold value to indicate the duration of pinning. Given the crack was seen to be pinned for up to 4000 cycles at a single location, the actual propagation rate at which the crack was propagating varied over a wide range as can be seen in Table 2. Upon being released from a pinning location, the propagation rate does not appear to be related directly to either the ΔSa or the total number of cycles.

4.2.2.1 Crack path prediction

Investigating the surface morphology changes on the sample surface in the vicinity of pinned cracks showed that while the building of a mound is always associated with a pinned crack, a local minimum is often created through which the crack eventually propagates (74). Figure 4-15a shows a difference image calculated for a pinned crack, which clearly shows a large mound being built adjacent to the crack tip. What can also be seen from Figure 4-15a is a valley forming on the other side of this mound, ultimately this valley was found to correspond with the crack path. Analysis showed that while the majority of surface roughness changes were constrained to the vicinity adjacent to the tip of the propagating crack, some surface roughness changes were measurable ahead of the crack.

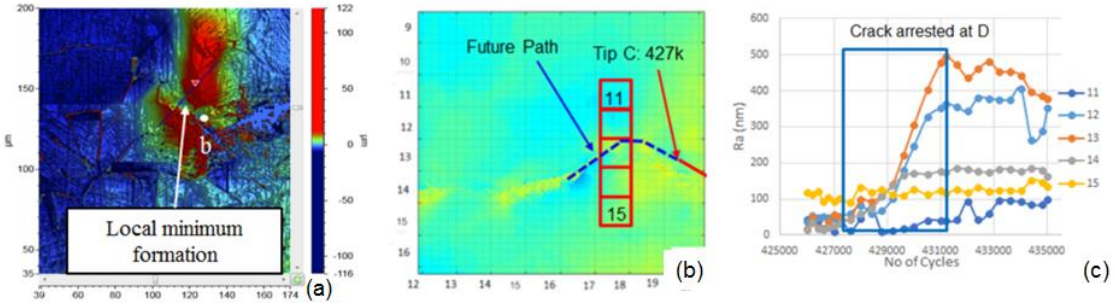

Figure 4-15 a) difference image of crack pinned a point A. b) Sub sets for which S_a and S_q were calculated ahead of pinned crack. c) S_a and S_q values for subsets as a function of cycles.

It was hypothesized that the amount of change for the area through which the crack would eventually propagate is higher than the surrounding areas (75). Figure 4-15b and 4-15c shows the changes at a sub-region close to the future path of the crack are high, and their magnitude vanishes in directions parallel to this future crack path. In order to predict crack paths from WLI images the following procedure was developed.

First, difference images, D_n , were calculated starting with the crack in a given reference location. While this reference can be any location, it was found to work best while a crack was pinned, or as a crack leaves a pinning location. Then absolute surface index images ΔS_n, where S_n is a surface index measurement, e.g. S_a and S_q, are calculated. These images were calculated by segmenting the difference images into sub regions of a given number of pixels and the surface index calculated for each sub region. Because these ΔS_n images are calculated from a difference image, they are actually measuring $\Delta S_n/\Delta Cycle$. As can be seen from Figure 4-15c, at distances far from the crack tip the slope of the *S* vs C_y curve for the sub-regions near the eventual path start changing more than the random fluctuations of sub-regions above and below. This allows for an interpolation method linearly connecting high points as the crack path prediction.

While the difference images are essentially normally distributed, it was found that the ΔS images fit a Weibull distribution very well as seen in Fig. 4.16 a shows a raw ΔS image for the area containing crack pinning locations A through E. An area of high contrast can be seen in the upper left corner. This high contrast was found to come from missing data in the WLI data due to a pit in the sample. Fig 4-16b shows the corresponding histogram. In the histogram, artifacts from the missing data can clearly be seen, as can the underlying Weibull distribution. In order to increase contrast of the actual crack path, first these measurement artifacts were manually masked. Next, considering those pixels with a lower $\Delta S/\Delta Cy$ do not contribute to the prediction of the crack path, this distribution could be used to calculate a threshold retaining only those pixels with the highest $\Delta S/\Delta Cy$ which should be most significant to the future path of the crack.

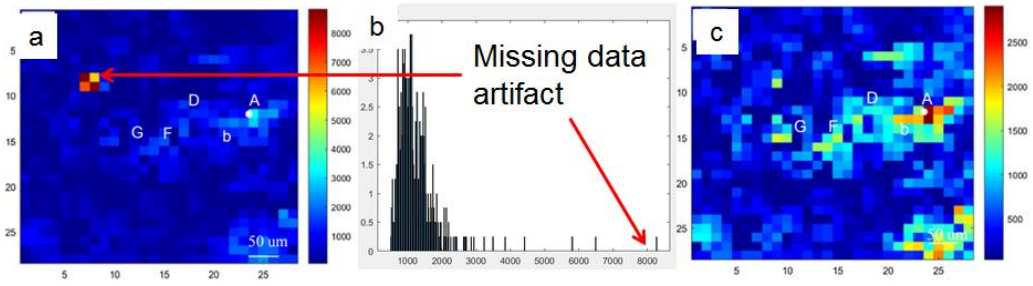

Figure 4-16 a) Raw ΔS images for the area containing the crack while pinned at point A. b) Histogram of raw ΔS images. c) ΔS image with artifacts removed and applied Weibull filter.

Setting the threshold to keep the upper 10% of *ΔS/ΔCy* values was seen to provide the best prediction threshold. In each step, *ΔS/ΔCy* pixels having less than 10% of the average threshold for $\Delta S_a/\Delta Cy$ and $\Delta S_t/\Delta Cy$ were excluded from the analysis, creating a binary image, B_n, containing only sub matrices for those values above the threshold as seen in Fig. 4-16 c. This process would be repeated for as many separate difference images as desired.

Next, unlike areas above and below the future path of the crack, the *ΔS/ΔCy* for the crack path is monotonically increasing, and should be evident in more images than the randomly fluctuating areas. In order to ensure each threshold value was contributing to the crack propagation a composite binary image C_n was calculated such that only sub matrices exceeding the threshold value in more than 50% of the images were retained. Finally the composite *ΔS/ΔCy* image was calculated as in equation 8.

(8)

$$\Delta S_c = C_n(i,j) * \Delta S_f(i,j)$$

In equation 8, ΔSf is the last ΔS/ΔCy image used in calculating the composite images. Upon calculation of this composite ΔSc image the linear interpolation method connecting high points was used as the crack path prediction.

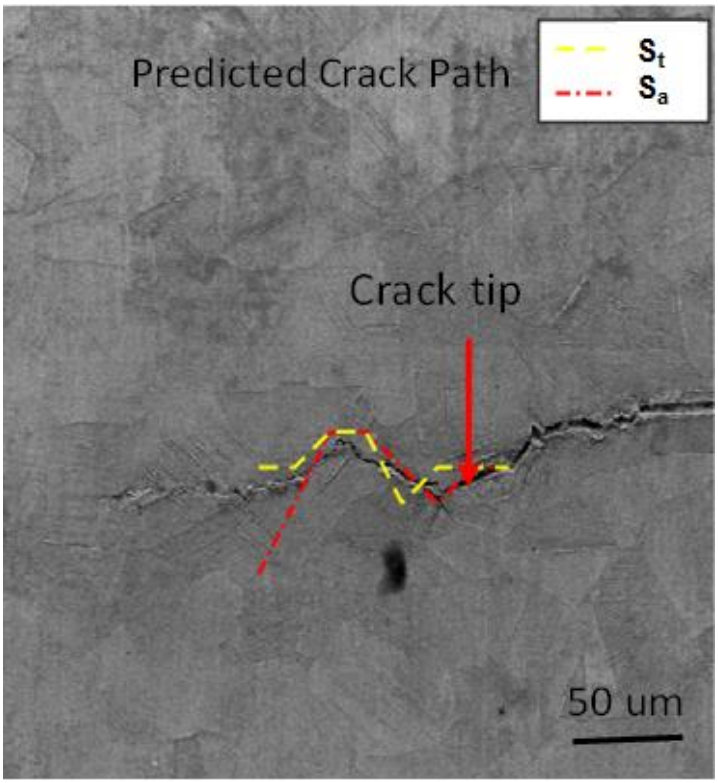

Figure 4-17. Predicted path in overlap zone, using 50X images, when crack arrested at point A (74).

Figure 4-17 shows the crack path predicted when the crack was pinned at point A. The procedure described above shows good agreement with the crack for 80 um ahead of the crack path.

4.2.3.1 EBSD/WLI crack path

As stated before, it is assumed that the structures visible to the WLI are caused by strain within the bulk interacting with the surface. Thus, the higher amount of surface roughness

changes seen around pinned cracks would indicate a higher amount of total plastic strain is needed for areas where the crack is pinned as opposed to the areas where the crack is propagating. In order to qualitatively correlate the amount surface changes to plastic strain, EBSD images were taken of an area of the EBSD/WLI sample once a full thickness crack was created. Due to lessons learned in the original study, and time constraints due to the much longer fatigue life of the EBSD sample WLI and EBSD images were analyzed as soon as a full though thickness crack was formed, without the 1.5 mm homogenization process.

For the crack propagation correlation study the same sample as the initiation study was used. Thus difference images as described above were available from 10,000 to 160,000 cycles. Figure 4-18 shows the 100,000 cycle difference image along with the 100,000 SEM image. In Figure 4-18a, is the 100,000 cycle difference image in which the future crack can clearly be seen; however, in Figure 4-18b the SEM image for the same number of cycles, it can clearly be seen that no surface crack has yet been initiated on the surface.

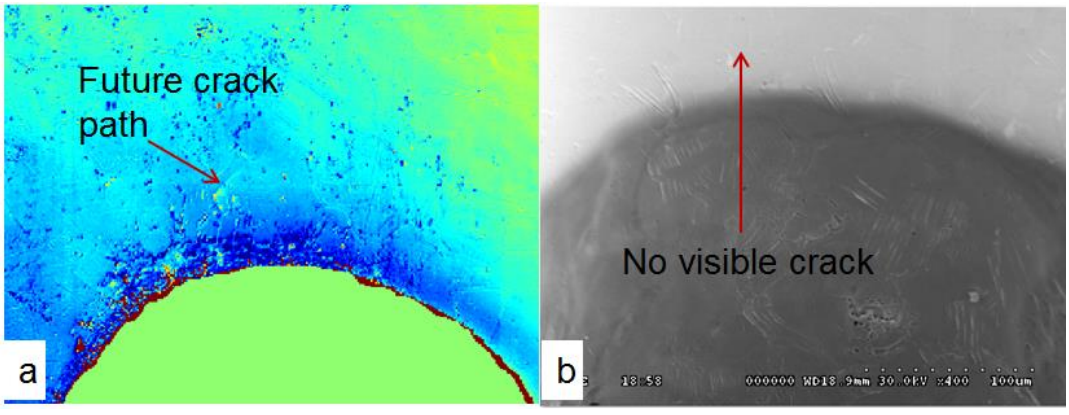

Figure 4-18 a) 100,000cycle WLI difference image showing the future path of the crack. b) 100,000cycle SEM image showing that the crack path visible in the difference image is not yet visible on the surface.

Over the next 45,000 cycles the crack was seen to grow from the notch to a total length of 129 um.

By 145,000 cycles it was clear that the nucleated crack was indeed the main macro crack. At 165,000 cycles the crack was seen to be pinned. Figure 4-19 shows the SEM and WLI image for the crack at 160,000 cycles. As has been seen before, the large red area seen in Figure 4-19b is obviously a crack at a pinned location.

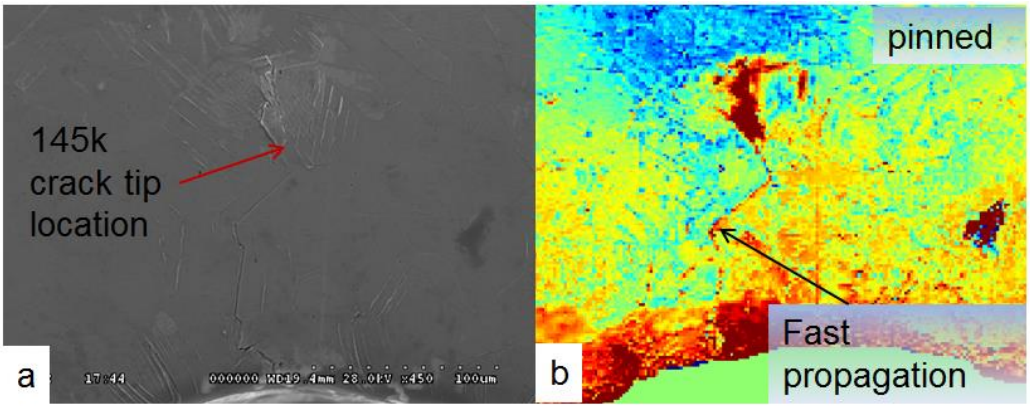

Figure 4-19 a) 160,000cycle SEM image with the 145,000cycle crack tip location indicated by the arrow. b) 160,000cycle WLI difference image showing the fast propagation area of the crack and the pinned area at the end of the crack.

At this point EBSD observations were shifted to the crack tip area. Due to surface roughness changes combined with contamination, oxide development and carbon deposition the quality of EBSD images had diminished substantially. In order to image the area at the crack tip, it became necessary to re-polish the sample between EBSD images. This re-polish was done very gently, first with a mechanical polish with 0.05 um alumina powder, only to remove the deposited carbon, then a 3 second flash electro polish. This procedure was done at 160,000 and 180,000 cycles. Due to this re-polish, the hill built between 140,000 and 160,000 cycles

was removed. For this reason there was no need to create a difference image between 160,000 and 180,000 as the difference between the surface profiles of the crack tip was clear in the WLI images. Figure 4-20a shows the WLI image for the crack tip at 160,000 cycles after electro polishing. Figure 4-20b shows the same area at 180,000 cycles before electro polishing. A small hill can be seen, and the crack is obviously still pinned close to the same area as in 160,000 advancing only 30 um in 20,000 cycles.

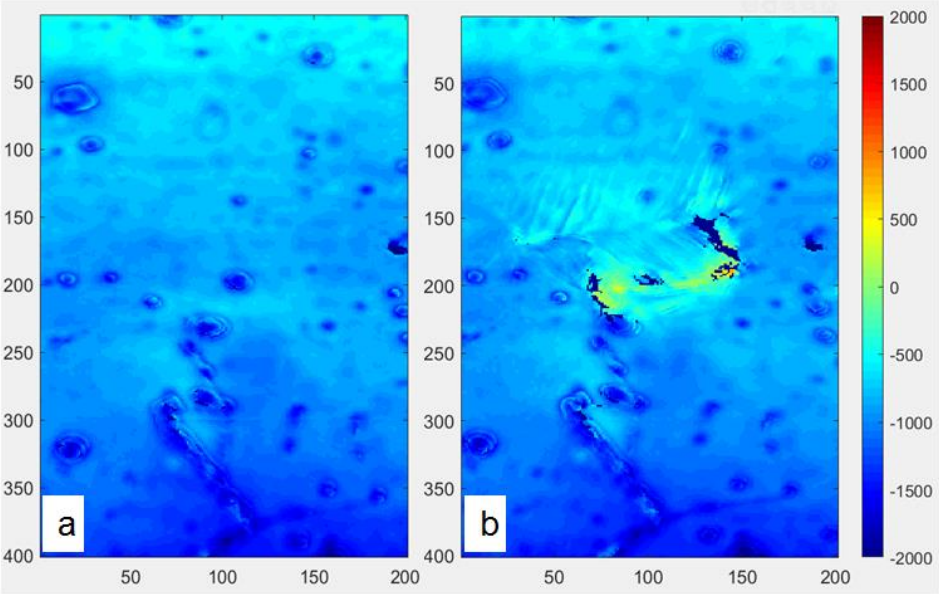

Figure 4-20 a) 160,000cycle WLI image taken after flash electro-polish. b) 180,000cycle WLI image taken before electro-polish.

In order to correlate surface roughness changes with strain localization around the crack tip, a procedure used by Rui et al was used (76; 77). The first step in this method is to calculate KAM images from EBSD images. Then a KAM vs. distance from the crack is calculated, ΔKAM. This distribution calculation is shown in Figure 4-21 (76). Over a relatively short section of the crack length, KAM measurements are taken at each pixel offset normal to the crack path, i.e. the

$N\Delta a_m$ values in Figure 4-21. Then, along distances parallel to the crack path the $N\Delta a_m$ values are averaged over m values.

Figure 4-21 Schematic representation of the post mortem crack path analysis proposed by Rui et al (76).

Figure 4-22a shows the 180,000 WLI image at the end of the crack. Figure 4-22b shows the KAM image overlaid on the SEM image for the same number of cycles. In Figure 4-22b two areas of the crack are marked. First the end of the crack, coincident with the pinning location, and second the Start of the crack which was the propagating portion of the crack. Figure 4-22c, shows the ΔKAM curves calculated for each crack section. While the absolute value of the KAM curves for the end of the crack is larger, it was shown by Rui et al that the maximum of the height for the KAM curve is linearly dependent on ΔK. The change difference in height of the Start and End portions of the crack was found to be explained completely by height the difference in ΔK due to the change in crack length; however, the width and non-symmetrical shape of the end curve are not explained by the rise in ΔK. While the absolute value of KAM may only be ΔK dependent, the volume over which increased strain is manifested may be microstructurally dependent, at least for mode I cracks.

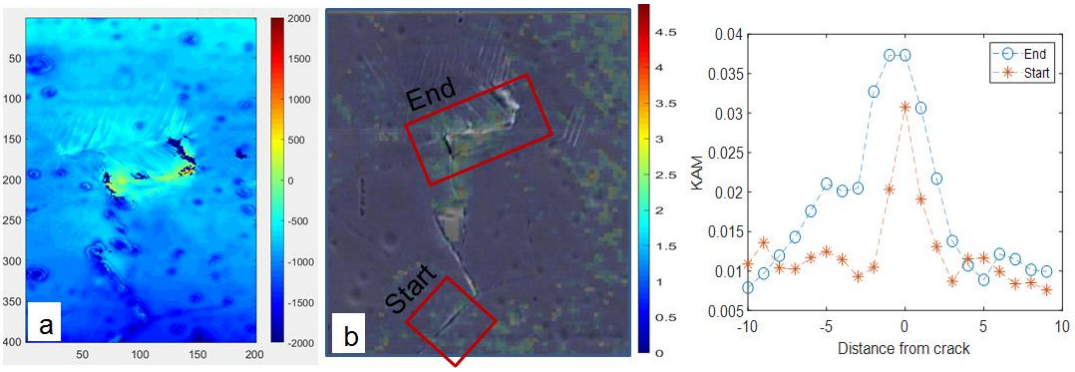

Figure 4-22 a) 180,000cycle WLI image of end of the crack path. b) 180,000cycle KAM measurement overlaid on SEM image. c) 180,000cycles KAM curves for the Start area, (propagating crack) and End area (pinned crack).

Because the GND density, equation 7, is directly proportional to KAM, higher values of KAM over a larger amount of volume would suggest a larger amount of strain energy is needed to advance a crack past a pinning location relative to a propagating crack.

4.3. Crack initiation

It has been noted that once a measurable macro crack is detected in nickel alloys, upwards of 70% of the fatigue life has been expended (78). This makes crack initiation at least as important a technical issue as crack propagation. In order to investigate the effect on surface features due to crack initiation two experiments were performed. First, the initial experiment was performed with a sample with the geometry and grain-sized material as described as the initial fatigue sample in table 1. This experiment was performed on Bose test bench with the in situ WLI. Second, in order to corroborate these results, and compare the surface topology technique to qualitative EBSD strain measurements a second experiment was performed with a sample of slightly different geometry, and grain size described as WBSD/WLI in table 1.

4.3.1 Initial crack initiation location determination

The techniques described below were used by Fathi et al to predict crack initiation sites at the root of crack tips (79). The initiation experiment was concerned with the root of the notch; therefore this area was not masked during electro polishing. As can be seen in the cross section at the notch root electro-polishing caused the root of the notch to be rounded. Also unlike the crack propagation studies, not knowing exactly where the crack would initiate necessitated imaging a much larger area. It was noticed after the first cycle a large plastic zone developed at the tip of the notch. Figure 4-23 shows the tip of the notch after the first applied cycle, showing the plastic zone within the analysis area taking on a more or less "saddle" shape.

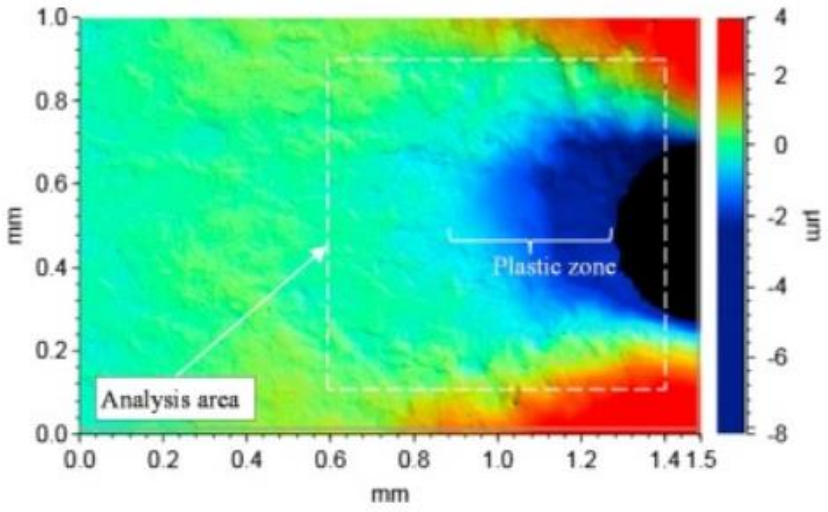

Figure 4-23 Root of the notch taken with the 10X WLI lens after the first cycle was applied (79).

It was found that due to this large plastic deformation, the tilt and z level corrections used in the previous studies, which were done on an essentially flat area, were not consistent. It became necessary to include a section in each image which was yet to be affected by plastic

deformation. In order to be able to image the entire notch, yet still be able to process the images so that acceptable difference images could be calculated, an area 0.8 x 0.8 mm was chosen to be imaged with the SWL 50X lens per the schedule indicated in table 3. Because it was seen that the WLI camera, and surface topology images do not always allow for unambiguous identification of crack locations an SEM imaging schedule was also created. At times indicated in Table 3 the sample was removed from the testing machine and the area of the notch was imaged. Not only was the surface of the sample visible to the WLI imaged, but also the root of the notch.

Table 3 WLI and SEM imaging schedules. Units are in cycles (79).

Fatigue cycle	Imaging interval	
	SWLI	SEM
0	1	1
1	1	1
1–1000	Every 200	None
1000–5000	Every 500	None
5000–20,000	Every 1000	At 20,000
20,000–40,000	Every 2000	At 40,000
40,000–60,000	Every 1000	Every 10,000
60,000–95,000	Every 500	Every 10,000

Because of the large initial plastic zone and rounded character of the notch it was found that using the entire image for registration produced very low quality difference images with large registration errors. This was due to the majority of registration points being concentrated around the notch. Also because of the angle at which these points were measured, they were often erroneous. The same area used for tilt compensation was used to calculate the transformation for registration of the entire image. Difference images were then calculated

using the WLI image taken after the first cycle as the reference image for all subsequent difference image calculations.

Once the difference images were calculated, ΔSa images were calculated as seen in Figure 4-16. Much like with ΔR images calculated for crack path calculations, areas of extremely high ΔSa were seen. Figure 4-24a shows the raw ΔSa for a crack initiation delta image. At the root of the notch very large ΔSa values can be seen. At the root of the notch tilt and registration errors were seen to be greatly magnified, thus like the missing data artifacts found in the crack propagation study these areas were manually removed. After removal of the high image registration artifacts the Sa distribution was once again seen to be Weibull, as seen in Figure 4-24b, so once again the Weibull filter was applied to create the final ΔSa images as seen in Figure 4-24c.

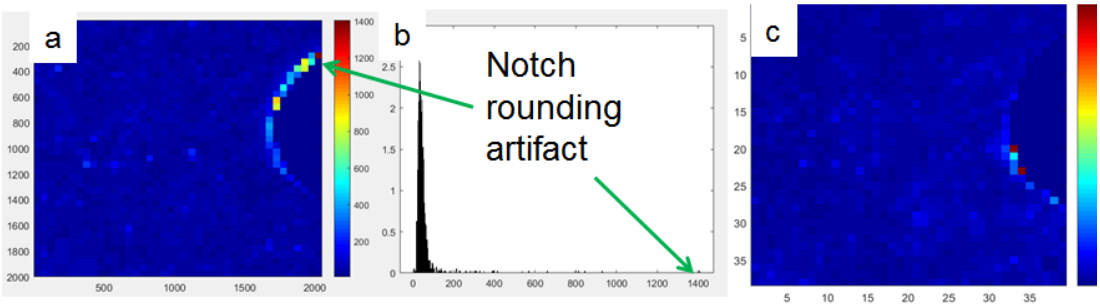

Figure 4-24 a) Raw ΔS images for the area close to the notch for initiation experiment. b) Histogram of raw ΔS images. c) ΔS image with artifacts removed and applied Weibull filter.

From the first cycle several areas of slip banding could be seen on the area around the notch; and these areas were indeed seen to correspond to hot spots in the ΔSa images. By 20,000 cycles a clearly visible "hotspot was seen in the ΔSa images. Once a suspected crack initiation location was identified SEM images were taken to verify crack development in order to

confirm ΔSa results. Figure 4-25a shows the 20,000 cycle ΔSa images with the SEM micrograph of the hot spot area. By 40,000 cycles, a surface crack had developed at the hot spot location. By 50,000 cycles the surface crack was seen, via SEM to be joining with a crack which had nucleated on the root of the notch Figure 4-25b. By 95,000 cycles the crack was verified by SEM to be a full thickness and was propagating from the hot spot nucleation location.

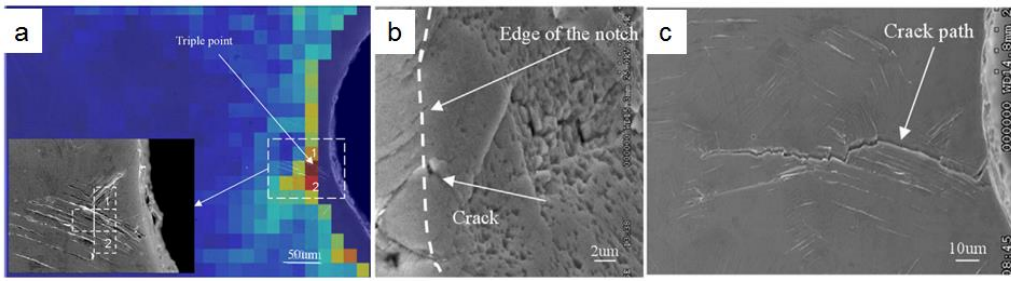

Figure 4-25 a) 40,000cycle ΔS_a image with SEM inset of the hotspot area. b) SEM image of the edge of the notch showing the surface crack connected to a crack on the root of the notch. c) SEM image of notch at 95,000 cycles.

Thus, the WLI ΔSa damage index method shown to be useful in predicting the mode I crack path, was shown to also be able to predict crack initiation locations relatively early compared to the fatigue life of the sample.

4.3.2 Crack initiation EBSD/WLI correlation

As seen in both the initiation and crack propagation studies previously described, the ΔSa damage index method seemed to rely on areas of heavy slip banding for determining crack behavior. In order to at least qualitatively correlate the ΔSa damage index method to relative strain for pinned and propagating cracks, a second center notch sample was made to the geometry as described for the EBSD/WLI sample in table 1. This sample was machined from a second sheet of nickel 200 with a measured average grain diameter of 50um.

For initiation and propagation studies performed with samples of the original geometry, the ΔK for initiation was limited by the loading capacity of the fatigue testing machine at approximately 11.2 MPa√m. Thus for the EBSD/WLI correlation sample the load was adjusted down in order to maintain the same initiation ΔK as in the original experiment. Lower load, combined with the smaller grain size essentially doubled the fatigue life of the EBSD/WLI sample. While the original samples had a measurable, through thickness crack at approximately 90,000 cycles, the EBSD/WLI sample did not have a similar crack until 180,000 cycles.

For the initial experiment a tremendous amount of images were taken. Experience gained suggested fewer WLI images were needed so an abbreviated schedule was used for the EBSD/WIL sample. WIL images were taken at 0 and 1 cycle, then every 10,000 cycles. SEM and EBSD images were taken initially and then every 20,000 cycles. An EBSD image was not possible to take at 80,000 due to SEM maintenance issues.

By 40,000 cycles two main areas of slip banding were visible to the WLI; when imaged by the SEM, slip banding was seen to be much more intense on the surface common to the root of the notch. At 40,000 cycles EBSD images were taken at 500x with an excitation voltage of 30kV. From 40,000 to 100,000 cycles no new slip band areas were seen to form on the area visible to the WLI. At 120,000 cycles a crack was nucleated on the surface of the sample and became a full thickness crack by 180,000 cycles. Figure 4-26 Shows the 40,000 SEM image with the future crack path traced by a red line. A smaller red line indicates the position of a

small crack which was seen to not propagate. Below the crack, on the root of the notch, a small crack can be seen to be nucleating. The inset highlighted in blue shows this crack at 120,000 and it can be seen to be linking with a crack on the surface which did not exist at 40,000. Thus, the initiation site was not associated with a large number of slip bands on the surface visible to the WLI.

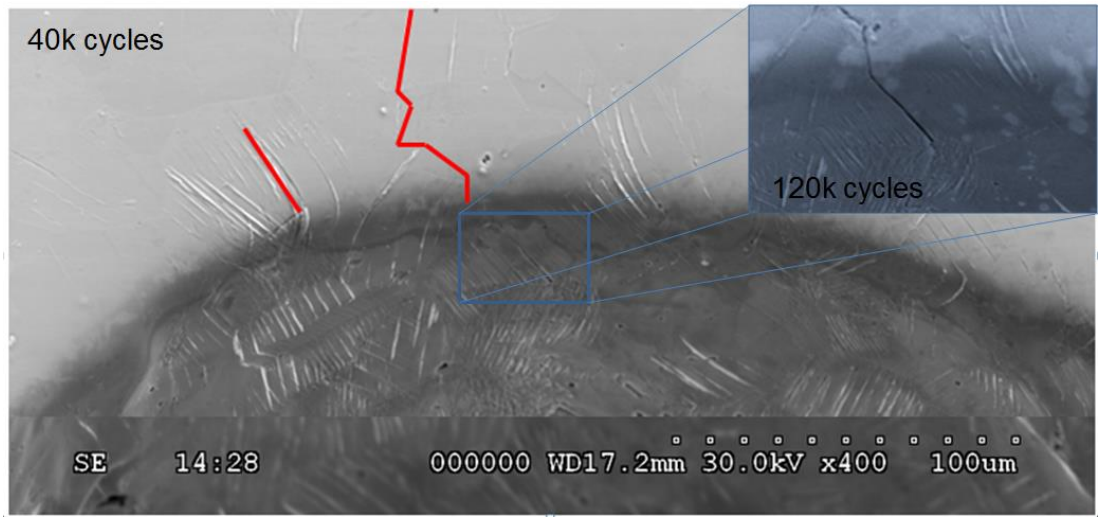

Figure 4-26 SEM image 40,000cycles with the future crack shown in red. Inset is the 120,000 cycle SEM image showing the crack on the root of the notch.

Figure 4-27 shows the ΔSa image for the notch at 50,000 cycles with the future crack path indicated in red.

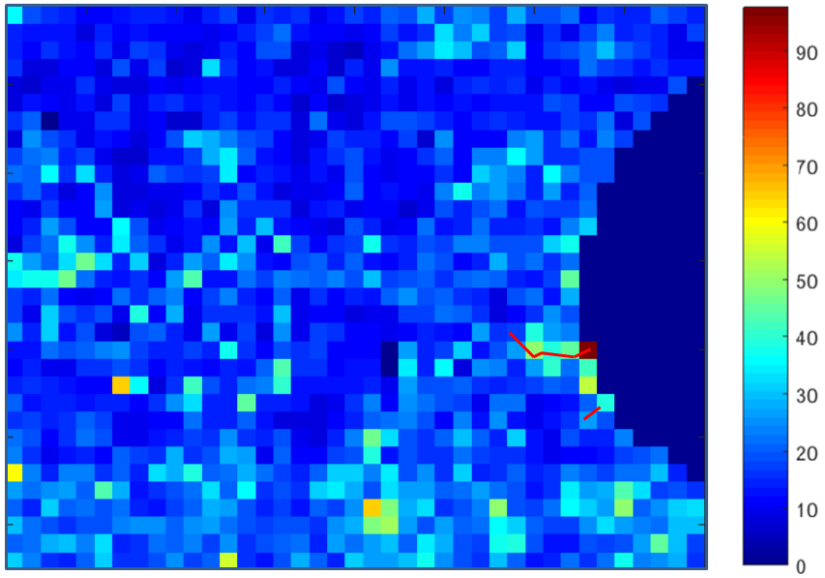

Figure 4-27 50,000 ΔS_a image with the future crack path indicated in red.

The hot spot seen in Figure 4-27 persisted throughout the remainder of the experiment, indicating that the ΔSa damage index for crack initiation may not be solely dependent on slip banding.

As discussed in section 2.2.1 EBSD imaging is very sensitive to the sample surface condition and can be affected by oxide development, contamination and after repeated EBSD measurements, carbon deposition. These effects were exacerbated in the current study as no attempts could be made, save sonicating in acetonitrile, to prep the sample surface between EBSD images due to fear of damaging the surface features being measured by the WLI. Thus EBSD image quality diminished quite severally early on.

Figures 4-28 a-c shows EBSD IQ and orientation images. It can be seen that while IQ stayed relatively high, the measured diffraction patterns could no longer be indexed in the area near the crack initiation locations. Due to the deterioration of the indexing kernel methods as described in section 2.2.3 could not be used between the cycles in which the crack initiated.

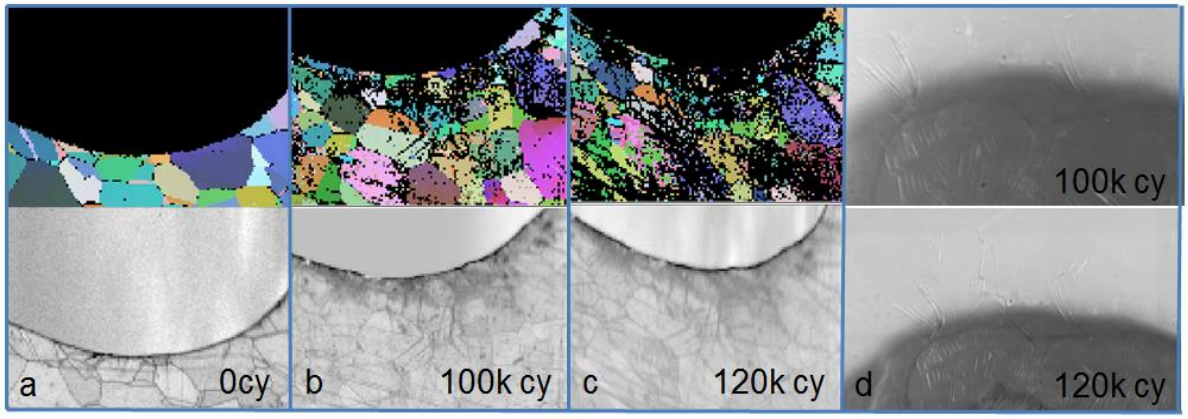

Figure 4-28 a-c) EBSD IQ and orientation maps at the indicated cycles. d) SEM images at 100k and 120k cycles over which the crack became visible on the surface of the sample.

Because kernel methods could not be used the crack path was compared to IQt, which has been shown to be sensitive to plastic strain. Figure 4-29 shows the crack location overlaid on the 120,000 SEM image. The inset shows the crack overlaid on the 120,000 EBSD image. In the IQ image, darker areas indicate a reduction in IQt. While there is some darkening of the image around the crack initiation location, the majority of IQt reduction was seen in the areas with slip banding. This indicates that while IQt may be the quality measure with the highest relative sensitivity to plastic strain, it is still sensitive enough to surface roughness changes for comparison to WLI data.

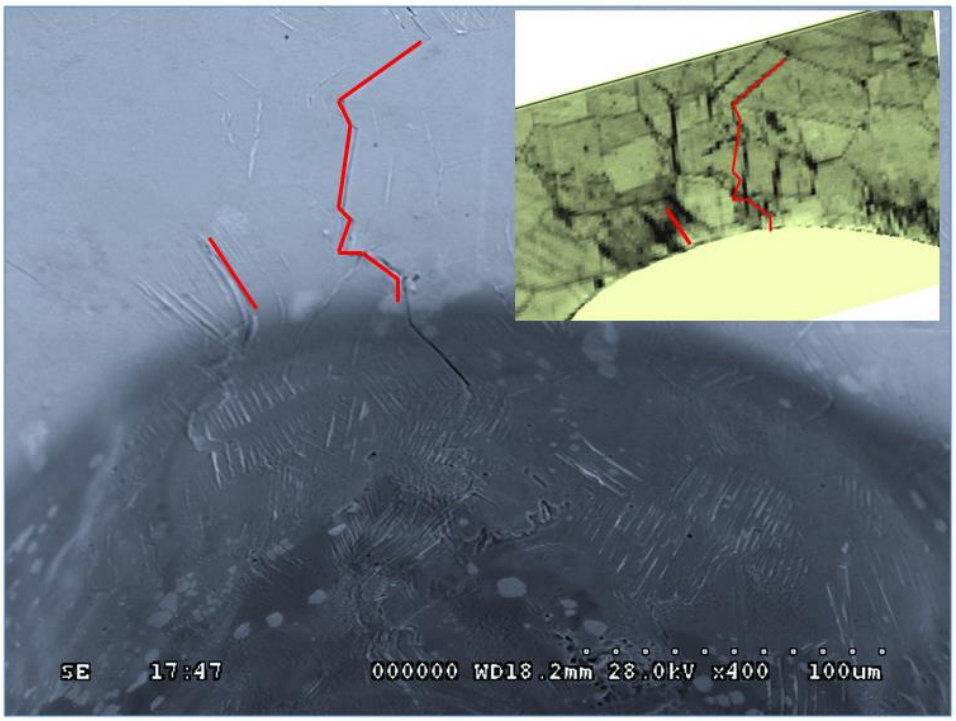

Figure 4-29 120k SEM image with crack path marked in red. Inset is the 120k IQ map with the crack path indicated in red.

Despite the poor quality of higher cycle EBSD images KAM images were calculated, via the MTex toolbox for Matlab, for the initial and 20,000 cycle images. Figure 4-25a is the KAM image with a 5 degree grain boundary threshold. Figure 4-25b is the KAM image for the same area at 20,000 cycles. A hotspot in KAM values is clearly seen at the crack initiation site. Thus while IQ techniques are not adequate for determining crack initiation locations, KAM clearly shows the crack initiation site before the ΔSa damage parameter.

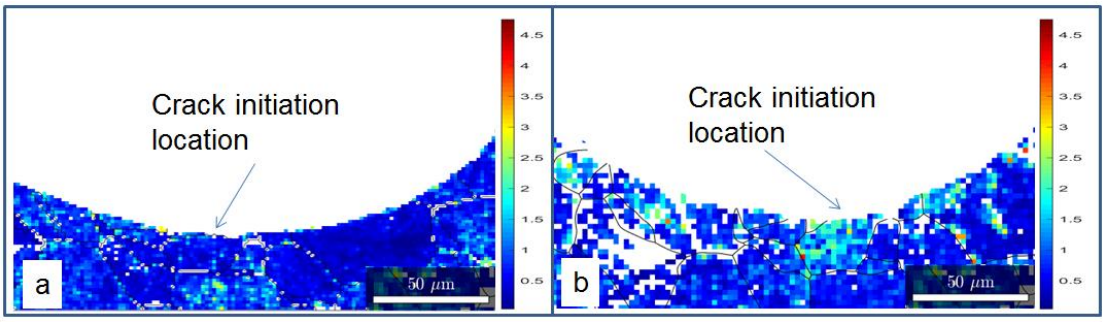

Figure 4-30 a) Initial KAM image with crack initiation area highlighted by the arrow. b) 20,000cycle KAM image with the crack initiation location indicated by the arrow.

Chapter 5 Conclusion

A simple, yet effective image processing technique was developed in order to quantify surface morphology changes in areas around the crack tip when the crack was propagated under fatigue loading. It was found that both the monotonic and cyclic plastic zones have a measurable effect on surface roughness of propagating cracks, which can be measured at a distance close to their respective theoretical sizes. Furthermore when a crack is pinned the most significant surface roughness changes can be measured close to the crack tip within the cyclic plastic zone.

It was also shown that the crack's future path is related to the changes in surface indexes such as Sa and St. These values where then used as a damage parameter incorporated into a method developed to predict the crack path. This method was found to be applicable through a wide range of WLI image resolution. The method showed good agreement between the predicted and actual paths for 130 um when the crack is pinned, and 100um for propagating cracks. The St surface index was found to provide a better prediction of the crack's future path. Using KAM based kernel methods verified that in areas where hills are built at crack pinning locations strain evolves over a larger volume around the crack path. Thus total strain energy is higher for pinned cracks vs propagating cracks.

EBSD kernel techniques were then used to verify that areas directly affected by the crack path experience much higher strain. This indicates that the WLI damage parameters, relative to

propagating and pinned cracks, do measure the areas within the cyclic plastic zone experiencing the highest cumulative strain. It was also seen that WLI difference images can sometimes clearly delineate the future crack path long before the crack or any slip banding is visible on the surface. This indicates that, at least for initiation of cracks, not all indications measured by the ΔSa damage parameters may be related to plastic strain directly observable to the WLI.

Chapter 6 Bibliography

1. Use of Dynamic Speckle Interferometry for Contactless Diagnostics of Fatigue Crack Initiation and Determining Its Growth Rate., A P Vladimirov, I S Kamantsev, V E Veselova, E S Gorkunov, S V Gladkovskii, 2016, Technical Physics Vol 61-4 563-568.

2. Study of the surface roughness evaluation of pinned cracks., R. Kelton, J. Fathi, E. Meletis, H. Huang, Paper No. IMECE2017-70729, pp. V009T12A007; 5 pages.

3. On the Relationship Between Deformation-Induced SurfaceRoughness and Plastic Strain in AA5052—Is it Really Linear?, M.R. STOUDT, J.B. HUBBARD, S.D. LEIGH, 2011 The Minerals, Metals & Materials Society Vol 42A(9) 2668-2679.

4. Quantitative study of surface roughness evolution during low-cycle fatigue of 316L stainless steel using Scanning White light Interferometric (SWLI) Microscopy., Y. Wang, E. Meletis, H. Huang, 2013 International Journal of Fatigue Vol 48 280-288.

5. A physically based fatigue model for prediction of crack initiation from persistent slip bands in polycrystals., Michael D. Sangid, Hans J. Maier, Huseyin Sehitoglu, 2011 Acta Materialia, vol 59-1 328-341.

6. The exponential law of endurance tests., O.H. Basquin, 1910 Proc. ASTM Vol 10 625-630.

7. The historical development of our understanding of fracture., George R Irwin, 1997 TMS annual meeting.

8. Methods to reduce the thermal conductivity of EB-PVD TBCs., J.R. Nicholls, K.J. Lawson, A. Johnstone, D.S. Rickerby, 2002 Surface and Coatings Technology Vol 151 383-391.

9. On the finite element modeling of fatigue crack growth in pressurized cylindrical shells., C.H.Furukawa, M.L.Bucalem, I.J.G.Mazell, 2009 International Journal of Fatigue Vol 31-4 629-635.

10. A rational analytic theory of fatigue., M. P. Gomez, W. E. A. Anderson,1961 Trends Eng. Vol 13 9–14.

11. A critical analysis of crack propagation laws. Paris, P., Erdogan, F, 1963 J. Basic Eng. Trans. ASME, Vol 85-4 528–534.

12. Barsom, Stanley T. Rolfe John M. Fracture and fatigue control in structures. englewood cliffs NJ: Prentice-Hall, 1977.

13. Wanhill, H.L. Ewalds R.J.H. Fracture mechanics. Victoria: Edward Arnold, 1983.

14. Some Remarks on the History of Fracture., Gross, Dietmar, 2014 Lecture Notes in Applied Mathematics and Mechanics, vol 1 195-209.

15. Introduction to the Long Life Bridges Project., E.J. OBrien, A.J. O'Connor and J.E. Arrigan, 2011 Bridge Maintenance, Safety, Management, Resilience and Sustainability Stresa Italy.

16. Suresh. Fatigue of materials. Cambridge : Cambridge University Press, 1998.

17. On the Beauty of Analytical Models for Fatigue Crack Propagation and Fracture—A Personal Historical Review., K. Schwalbe, 2010 Fatigue and Fracture Mechanics Vol 7(8).

18. Scaling phenomena in fatigue and fracture., G. I. Barenblatt, 2006 International journal of fracture 138:19.

19. Correlation between dislocation organization and slip bands: TEM and AFM investigations in hydrogen-containing nickel and nickel–chromium., G. Girardin, C. Huvier, D. Delafosse, X. Feaugas, 2015 Acta Materialia Vol 91 141-151.

20. Dieter, George E. Mechanical metallurgy. s.l. : McGraw-Hill, 1986.

21. Orientation-dependent evolution of the dislocation densityin grain populations with different crystallographic orientations relativeto the tensile axis in a polycrystalline aggregate of stainless steel,. Tamas Ungar, Alexandru D. Stoica, Geza Tichy, Xun-Li Wang, 2014 Acta Materialia Vol 66 251-261.

22. Plastic behavior of a nickel-based alloy undermonotonic-tension and low-cycle-fatigue loading., E-Wen Huang, Rozaliya I.Barabash, Yandong Wang, Bjørn Clausen, Li Li, Peter K. Liaw, Gene E. Ice, Yang Ren, Hahn Choo, Lee M. Pike, Dwaine L. Klarstrom,. Vol. 2008 International Journal of Plastisity Vol 24 1440-1456.

23. Modeling of residual stress relaxation of fatigue in 2024-T351 aluminium alloy., Omar Suliman Zaroog, Aidy Ali, B.B. Sahari, Rizal Zahari, 2011 International Journal of Fatigue Vol 33 279-285.

24. The study of dislocation structures at fatigue crack tips in polycrystalline copper under various crack propagation rates at stage II: crack propagation., H.L. Huang, N.J. Ho, W.B. Lin, 2000 Materials Science and Engineering Vol A279 261-265.

25. Dislocation structures around crack tips of fatigued polycrystalline copper., Yoshihisa Kaneko, Masao Ishikawa, Satoshi Hashimoto, 2005 Materials Science and Engineering Vol 400 418-421.

26. Dislocation structures in cyclically deformed nickel polycrystals., C. Buque, J. Bretschneider, A. Schwab, C. Holste, 2001 Materials Science and Engineering Vol A300 254-262.

27. Study of dislocation structures near fatigue cracks using electron channelling contrast imaging technique (ECCI)., J. Ahmed, A. J. Wilkinson, S. G. Roberts, 2003 Journal of Microscopy Vol 195(3) 197-203.

28. Application of the electron channeling contrast imaging technique to the study of dislocations associated with cracks in bulk specimens., B.C. Ng, B.A. Simkin, M.A. Crimp, 1998 Ultramicroscopy Vol 75 137-145.

29. Cyclic stress–strain behavior of polycrystalline nickel., Y. El-Madhoun, A. Mohamed, M.N. Bassim, 2004 Materials Science and Engineering A Vol 385 140-147.

30. Theory and application of electron channelling contrast imaging under controlled diffraction conditions., Nahid-Nora Elhami, Stefan Zaefferer, 2014 Acta Materialia Vol 75 20-50.

31. Coupling of Electron Channeling with EBSD: Toward the Quantitative Characterization of Deformation Structures in the SEM., Raabe, I. Gutierrez-Urrutia, S. Zaefferer, D Raabe., 2013 JOM Vol 65-9 1229-1236.

32. A Review of Strain Analysis Using Electron backscatter diffraction., Stuart I. Wright, Matthew M. Nowell, David P. Field, 2011 Microscopy and Microanalysis Vol 17 316-329.

33. Orientation gradients and geometrically necessary dislocations in ultrafine grained dual-phase steels studied by 2D and 3D EBSD., Marion Calcagnotto, Dirk Ponge, Eralp Demir, Dierk Raabe, 2010 Materials Science and Engineering A Vol 527 2738-2746.

34. A comparison of EBSD based strain indicators for the study of Fe-3Si steel., Claire Schayes, Jérémie Bouquerel, Jean-Bernard Vogt, Frédéric Palleschi, Stefan Zaefferer, 2016 Materials Characterization vol 116 61-70.

35. Observation of deformation and fracture heterogenities in a nickel-base superalloy using electron back scattering patterns., P.N. Quested, P.J. Henderson and M. McLean, 1988 Acta Metallurgica 36(10) 2743-2752.

36. A simple procedure for the assessment of plastic strain in electron back-scatter diffraction patterns., P.J. Buchanan, V. Randle, P.E.J. Flewitt, 1997 scripta materialia Vol 37-10 1511-1518.

37. Quantitative deformation studies using electron back scatter patterns., A.J. Wilkinson, D.J. Dingley, 1991 Acta Metallurgica et Materialia Vol 39 3047-3055.

38. Estimation of Elastic Strain by Integrated Image Correlation on Electron Diffraction Patterns., Qiwei Shi, Stéphane Roux, Felix Latourte, François Hild, 2019 Ultramicroscopy Vol 199 16-33.

39. Distribution of Local Deformations in Diamond Crystals According to the Analysis of Kikuchi Lines Profile Intensities., M. D. Borcha, S. V. Balovsyak, I. M. Fodchuk, V. N. Tkach, 2013 Journal of Superhard Material Vol 35 34-42.

40. Elastic strain tensor measurement using electron backscatter diffraction in the SEM., David J. Dingley, Angus J. Wilkinson, Graham Meaden, Phani S. Karamched, 2010 Journal of Electron Microscopy Vol 59 155-163.

41. A strain state in synthetic diamond crystals by the data of electron backscatter diffraction method., I. M. Fodchuk, M. D. Borcha, V. Yu. Khomenko, S. V. Balovsyak, V. M. Tkach, O. O. Statsenko, 2016 Journal of superhard materials Vol 38-4 271-276.

42. EBSD Image Quality Mapping., Stuart I. Wright and Matthew M. Nowell, 2006 Microscopy and microanalysis Vol 12-1 72-84.

43. Advances In automated EBSP single orientation measurement., K. Kunze, S. I. Wright, B. L. Adams, D. J. Dingley, 1993 Textures and Microstructures Vol 20 1-4 41-54.

44. Alternatives to Image Quality (IQ) Mapping in EBSD., Xiaodong Tao, Alwyn Eades, 2002 Microsc.Microanal Vol 8(suppl. 2)2.

45. An EBSD Study on Mapping of Small Orientation Differences in Lattice Mismatched Heterostructures., Xiaodong Tao, 2003 Dissertation Abstracts International Vol 64-12, Section: B, 6284.; 196.

46. Errors, Artifacts, and Improvements in EBSD Processing and Mapping., Xiaodong Tao, Alwyn Eades, 2005 Microscopy and Microanalysis Vol 11 79-87.

47. Overcoming the drawbacks of plastic strain estimation based on KAM., Rickard R. Shen, Pål Efsinga, 2018 Ultramicroscopy Vol 184A 156-163.

48. Fatigue damage assessment of alternator fans by EBSD., J.-B. Vogt, J. Bouquerel, F. Léaux, F. Palleschi, 2013 Procedia Engineering Vol 66 608-614.

49. Quantification of lead-free solder fatigue by EBSD analysis., T. Fujiwara, K. Yamamoto, H. Kimura, 2018 Microelectronics reliability Vol 88-90 691-694.

50. Measuring Plasticity with Orientation Contrast Microscopy in Aluminium 6061-T4., S. Ghodrat, A.C. Riemslag, L.A.I Kestens, 2017 Metlas Vol 7(4) 108.

51. Advanced analysis of crack tip plastic zone under cyclic loading, M. Besel., E. Breitbarth, 2016 International Journal of Fatigue Vol 93 92-108.

52. Investigation of the indentation size effect through the measurement of the geometrically necessary dislocations beneath small indents of different depths using EBSD tomography., Eralp Demir, Dierk Raabe, Nader Zaafarani, Stefan Zaefferer,. 2009 Acta Materialia Vol 57 559-569.

53. Local Plastic Strain Measurement by EBSD., M. Kamaya, J. Q. Da Fonseca, L. M. Li, M. Preuss., 2007 Applied mechanics and materials Vol 7-8 173-179.

54. Effects of LPSO/α-Mg interfaces on dynamic recrystallization behavior of Mg96.5Gd2.5Zn1 alloy., Yuanli Chen, Li Jin, Jie Dong, Fenghua Wang, Yangxin Li, Yanjun Li, Hongchen Pan, Xi Nie, 2017 Materials Characterization Vol 134 253-259.

55. Characterization of microstructural damage due to low-cycle fatigue by EBSD observation., M. Kamaya, 2009 MATERIALS CHARACTERIZATION Vol 60 1454-1462.

56. https://www.nobelprize.org/prizes/physics/1914/laue/biographical/ . [Online]

57. Williams, David B. Carter, C. Barry. Transmission electron microscopy : a textbook for materials science 2nd edition,. New York; London: Springer, 2009.

58. Digital direct electron imaging of energy-filtered electron backscatter diffraction patterns., S. Vespucci, A. Winkelmann, G. Naresh-Kumar, K. P. Mingard, D. Maneuski, P. R. Edwards, A. P. Day, V. O'Shea, and C. Trager-Cowan, 2015 Phys. Rev. B Vol 92 1-9.

59. Transmission Kikuchi diffraction in a scanning electron microscope: A Review., Glenn C. Sneddon, Patrick W. Trimby, Julie M. Cairney, 2016 Materials Science and Engineering R Vol 110 1–12.

60. A Dictionary Approach to Electron Backscatter Diffraction Indexing., Yu H. Chen, Se Un Park, Dennis Wei, Greg Newstadt, Michael A. Jackson, Jeff P. Simmons, 2015, Microscopy and Microanalysis, Volume 21(3) 739-752.

61. Schwartz, Robert A. Schwarzer David P. FieldBrent L. AdamsMukul KumarAdam J. Present State of Electron Backscatter Diffraction and Prospective Developments. Boston, Ma: Springer, 2009.

62. https://www.mathworks.com/help/images/radon-transform.html. [Online]

63. Dynamical Electron Backscatter Diffraction Patterns. Part I: Pattern Simulations., P. G. Callahan and M. De Graef, 2013 Microscopy and Microanalysis Vol 19 1255-1262.

64. Orientation averaging of electron backscattered diffraction data., F. J. Humphreys, P. S. Bate, P. J. Hurley, 2001 Journal of Microscopy Vol 201 50-58.

65. Denoising of Crystal Orientation Maps., Ralf Hielscher, Christian B Silbermann, Eric Schmidl, 2018, Unpublished. https://doi.org/10.13140/RG.2.2.13635.66088.

66. Characterization of tantalum nitride thin films synthesized by magnetron sputtering., Anna Zaman, 2014 ProQuest Dissertations And Theses Volume: 53-04.; 91p.

67. Surface topography evolution through production of aluminium offset lithographic plates., B. Rivett, E.V. Koroleva, F.J. Garcia-Garcia, J. Armstrong, G.E. Thompsona, P. Skeldona, 2010 Wear Vol 270 204-217.

68. White Light Interferometry., James C. Wyant, 2002 Proceedings of SPIE.

69. White Light Scanning Interferometry Based on Generalized Cross-Correlation Time Delay Estimation., Yunfei Zhou, Liyun Zhong, Hongzhi Cai, Jindong Tian, Dong Li, Xiaoxu Lu, 2017 IEEE photonics Vol 9(5).

70. The fundamental relationships between grain orientation, deformation-induced surface roughness and strain localization in an aluminum alloy., M R Stoudt, L E Levinea, A Creuziger, J B Hubbard, 2011 Material science and engineering Vol A530 107-116.

71. Cottrell, A. Dislocations and plastic flow in crystals. Oxford : Clarendon Press, 1953.

72. BRISK: Binary Robust invariant scalable keypoints., S. Leutenegger, M. Chli, R. Y. Siegwart, 2011 International Conference on Computer Vision.

73. SURF: Speeded Up Robust Features., H. Bay, T. Tuytelaars, L. V. Gool, 2006 Computer Vision ECCV 2006 Lecture Notes in Computer Science, 404-417.

74. CRACK GROWTH PATH PREDICTION BASED ON SURFACE ROUGHNESS EVOLUTION., Jalal Fathi Sola, Randall Kelton, Haiying Huang, Efstathios I. Meletis, 2017 MS&T Pittsburg.

75. A surface roughness based damage index for predicting future propagation path of microstructure-sensitive crack in pure nickel., Jalal Fathi Sola, Randall Kelton, Efstathios I. Meletis, Haiying Huang, 2019 international Journal of fatigue Vol 122 164-172.

76. EBSD analysis of cyclic load effect on final misorientation distribution of post-mortem low alloy steel: A new method for fatigue crack tip driving force prediction,. Shao-Shi Rui, Yi-Bo Shang,Yue Su Wenhui Qiu, Li-ShaNiu Hui-JiShi, Shunsaku Matsumoto, Yasuharu Chuman. 2018, International Journal of Fatigue Vol 113 264-276.

77. Fracture mode identification of low alloy steels and cast irons by electron back-scattered diffraction misorientation analysis., Shao-Shi Rui, Yi-Bo Shang, Wenhui Qiu, Li-Sha Niu, Hui-Ji Shi, Shunsaku Matsumoto, Yasuharu Chuman,. 2017 Journal of Materials Science & Technology Vol 33 1582-1595.

78. Investigation of small fatigue crack initiation and growth behaviour of nickel base superalloy GH4169., L. Zhu, Z. R. Wu, X. T. Hu, Y. D. Song, 2016 Fatigue & Fracture of Engineering Materials & Structures Vol 39.

79. Predicting crack initiation site in polycrystalline nickel through surface topography changes., Jalal Fathi Sola, Randall Kelton, Efstathios I. Meletis, Haiying Huang, 2019 International Journal of Fatigue Vol 124 70-81.

80. Visualization and Quantitative Analysis of Crack-Tip Plastic Zone in Pure Nickel., RANDALL KELTON, JALAL FATHI SOLA, EFSTATHIOS I. MELETIS, 2018 JOM Vol 70(7) 1175-1181.

Bio

Randall Kelton was born in 1975, in Chicago, Illinois. His family relocated to Texas when he was two. He grew up in Boyd, Texas where he graduated high school. Randall attended the University of North Texas from 2000 to 2003. He graduated cum laude, with a B.S. in Manufacturing Engineering becoming the first person in his family to obtain a college degree. After college, Randall worked in the aerospace and defense industry as a manufacturing, and later quality engineer for Vought Aircraft Industries, Inc. and Sikorsky Aircraft, Inc. His curiosity and scientific mind eventually led him back to the academic world. Randall began working on his PhD at the University of Texas in Arlington under the supervision of Dr. Estefanos Meletis in 2014. His research interests include near and far field surface changes induced by cyclic cracks in face centered cubic metallic materials, as well as corrosion evaluation of plasma process coating. While in the PhD program, Randall won the prestigious Kelcy Warren Graduate Fellowship for Engineering. He published five articles in some of the most respected journals for Material Science and Engineering. Randall taught undergraduate and graduate classes at both the University of Texas in Arlington and Texas Christian University. Randall is currently working as a process engineer at Pratt and Whitney, where he is responsible for development of thermal barrier coatings for high temperature turbine parts. Randall is married, with a son and two step daughters.

Publications to date

Visualization and Quantitative Analysis of Crack-Tip Plastic Zone in Pure Nickel. **RANDALL KELTON, JALAL FATHI SOLA, EFSTATHIOS I. MELETIS.** 7 , 2018, JOM, Vol. 70, pp. 1175-1181.

Predicting crack initiation site in polycrystalline nickel through surface topography changes. **Jalal Fathi Sola, Randall Kelton, Efstathios I. Meletis, Haiying Huang.** https://doi.org/10.1016/j.ijfatigue.2019.02.027, 70-81 : s.n., 2019, International Journal of Fatigue, Vol. 124, pp. 70-81.

A surface roughness based damage index for predicting future propagation path of microstructure-sensitive crack in pure nickel. **Jalal Fathi Sola, Randall Kelton, Efstathios I. Meletis, Haiying Huang.** https://doi.org/10.1016/j.ijfatigue.2019.01.012, 2019, international Journal of fatigue, Vol. 122, pp. 164-172.

Investigating the relationship between grain orientation and surface height changes in nickel polycrystals under tensile plastic deformation. **Kranthi Balusu, Randall Kelton, Efstathios I. Meletis, Haiying Huang.** https://doi.org/10.1016/j.mechmat.2019.04.011, Mechanics of Materials.

Conference papers

Kelton, R. F. (n.d.). “Study of the surface roughness evaluation of pinned cracks”. 2017: IMECE.

Jalal Fathi Sola, **Randall Kelton** (2017). “CRACK GROWTH PATH PREDICTION BASED ON SURFACE ROUGHNESS EVOLUTION”. Pittsburg.